



Hollow nanocage with skeleton Ni-Fe sulfides modified by N-doped carbon quantum dots for enhancing mass transfer for oxygen electrocatalysis in zinc-air battery

Rongyue Wang^a, Jin Liu^a, Jiahao Xie^a, Zhuang Cai^{a,*}, Yuan Yu^a, Zixuan Zhang^a, Xin Meng^a, Cheng Wang^{b,**}, Xiaoqin Xu^a, Jinlong Zou^{a,*}

^a Key Laboratory of Functional Inorganic Material Chemistry, Ministry of Education of the People's Republic of China, School of Chemistry and Materials Science, Heilongjiang University, Harbin 150080, China

^b School of Chemical Engineering and Light Industry, Guangdong University of Technology, Guangzhou 510006, China

ARTICLE INFO

Keywords:

Bifunctional oxygen catalyst
Bimetallic sulfide
Carbon quantum dots
Porous hollow nanocage
Synergistic effect

ABSTRACT

Constructing nonprecious-metal catalysts for oxygen reduction/evolution reactions (ORR/OER) in Zinc-air battery (ZAB) by structural regulation is crucial, but balance between stable structure and efficient mass transfer is still ambiguous. Here, hollow bimetallic sulfide nanocages with anchored N-doped carbon-quantum-dots are synthesized using a selective-etching method (Ni-Fe-S/NCQDs). The marked Ni-Fe-S/3NCQDs exhibits a promising half-wave potential of 0.85 V ($E_{1/2}$, ORR) and an excellent overpotential of 0.295 V at 10 mA cm⁻² (OER). Ni-Fe-S/3NCQDs has a negative $E_{1/2}$ shift of only 12.8 mV after 5000 cycles (ORR) and a current-density decline of only 7.05 % after 20 h tests (OER). Ni-Fe-S/3NCQDs with porous-hollow structure (478.35 m² g⁻¹) facilitates mass transfer and exposure of active-sites. Ni/Fe oxyhydroxides (in-situ X-ray diffraction) contributes to excellent OER activity/stability. ZAB with Ni-Fe-S/3NCQDs can be repeatedly charged and discharged for 240 h at 10 mA cm⁻². It provides a new strategy for constructing open-hollow structure to improve ORR/OER performances.

1. Introduction

Considering the increasing environmental pollution and fossil fuel exhaustion, renewable energy technologies such as fuel cells [1], solar cells [2], Li-ion batteries and metal-air batteries (MABs) should play important roles in many fields in the future [3,4]. The electrochemical reaction rate of MABs strongly depends on the oxygen reversible electrochemical process on the cathode, including oxygen reduction reaction (ORR) and oxygen evolution reaction (OER) [5,6]. However, the sluggish ORR/OER kinetics originated from complex multi-step electron transfer accompanied by depressed mass diffusion greatly impedes their further application [3,7,8]. Therefore, it is necessary to develop highly-efficient electrocatalysts for ORR/OER to promote the mass transfer efficiency and the reaction rate. In addition, it should be pointed out that as the ORR and OER occur under completely different conditions, especially the different electric potentials during the reactions, so the best ORR catalyst usually has poor OER activity, and vice versa [7–9]. Although a few materials can be developed used as bifunctional

electrocatalysts to catalyze these two reactions in MABs [9–11], the research of electrocatalyst with a superior durability for bifunctional activity in the same electrolyte is still a major challenge [8–13]. Therefore, various noble metal-free catalysts such as transition metals-derived nanomaterials (Co, Mn, Ni, Zn, etc.) and heteroatoms (N, P, S, etc.)-doped carbon materials have attracted more attention due to high ORR/OER activity and suitable economy [14–17].

Prussian blue (PB), with a face-centered cubic structure, can be transformed into a Prussian blue analog (M-PBA) materials through the coordination reaction of metal cations [18]. Due to the reversible insertion of ions into the open framework, which is coupled with the redox of structured metal cations, the PBA exhibits excellent electrochemical performance in alkali metal ion batteries [19–21]. Recent studies have shown that the conversion of nano-structured PBA into functional transition metal oxygen/non-oxide can retain its original nano-framework and improve catalytic performance by redistributing the electron density on the surface of the transition metal [19,21–24]. Huang et al. propose a straightforward strategy to construct CoFe-PBA

* Correspondence to: Xuefu Road 74#, Nangang District, Harbin 150080, China.

** Corresponding author.

E-mail addresses: hlju_chem218c@163.com (Z. Cai), wangc_93@gdut.edu.cn (C. Wang), zoujinlong@hlju.edu.cn (J. Zou).

by using co-precipitation method with the control of Co/Fe molar ratio, and the derived ternary Co-Fe-P shows a high catalytic activity for OER on glassy carbon electrode with an over-potential (η_{10}) of 235 mV [21]. Kahnamouei et al. prepare the NiCo-S@CoFeA-TT catalyst by pyrolyzing the cage-like CoFe-PBA with sulfuration, which shows a superior OER activity due to its abundant 3D diffusion channels and highly-dispersed metal sites [25]. As indicated, the large atomic radius of S atom (compared to B/N/P atoms) makes the M-S bonds weaker, which can drive the breaking process of more kinetically-favorable bonds for oxygen electrocatalysis [26,27]. This driving also leads to a fast charge transfer kinetics and highly-reversible electrochemical reactions [26, 27]. Briefly, these studies show the feasibility of converting CoFe-PBA to oxides, sulfides and other compounds by calcination to achieve excellent OER performance. However, the metal-ligand bonding is affected by the high temperature calcination, which makes the framework structure of PBA more fragile and reduces the active sites for ORR [15]. To maintain the advantage of the frameworks for oxygen electrocatalysis and improve the ORR activity of PBA-based catalyst, the cooperation of M1M2-PBA and carbon materials (including carbon nanotube, graphene, N-doped carbon quantum dots (NCQDs), etc.) may help the catalyst achieve a high bifunction [25,28,29].

Moreover, the open structure with highly porous skeleton is generally considered as an advantage over the solid structure to improve the electrocatalytic activity for ORR/OER [14,25]. The open structure can ensure the formation of a favorable catalytic interface among active sites, substrate and electrolyte, which significantly improves the electrocatalytic performance [30]. The high exposure of active sites, the strain-induced highly-reactive surface, and the increase of collision frequency by confining reactants within nanoscale spaces can all be realized in the open nanostructure [11,30]. Ren et al. propose a strategy to prepare the bimetal-based porous carbon nanorod (FeNiCo@NC-P) by using dual-MOF-hybrid ($\text{Fe}_2\text{NiMIL-88}@\text{ZnCoZIF}$). This porous catalyst shows an excellent bifunctional electrocatalytic activity (ORR/OER) in zinc-air battery (ZAB) [31]. Liang et al. use MOF nanocrystals as templates to prepare CoP-TiO_x hybrid materials for efficient and durable OER electrocatalysis. The introduction of TiO_x hollow nanocage with abundant Ti³⁺ sites can not only prevent the aggregation of CoP nanoparticles, but also promote the charge transport and change the electron density of CoP [32]. As mentioned above, an inspiration that combines the open porous structure derived from M1M2-PBA with NCQDs is brought to study the relationship between structure and bifunctional activity. The small-volume NCQDs with abundant oxygen-containing functional groups can be well dispersed on the surface of open pores to prevent the aggregation of NCQDs and the fast corrosion of M1M2-derivates.

Here, we report a combined structure of porous M1M2-sulfides open nanocages and small-sized NCQDs (Ni-Fe-S/NCQDs) for bifunctional electrocatalysis (ORR/OER). The NiS/FeS nanocage with hollow structure and multiple holes is obtained through ammonia selective etching of NiFe-PBA at room temperature. S element is more likely to induce the migration of electrons in the outer layer of the metal atom, leading to the change in the energy band structure of Fe/Ni species. Moreover, the S atom with excellent O-species affinity can endow the Ni-Fe-S species with moderate adsorption energies of O-intermediates to promote the charge activation to enhance ORR/OER activity. This porous structure facilitates the mass transport and the full utilization of electrolyte in ORR/OER. The internal cavity structure can reduce the possibility of the collapse of hollow nanostructure and stabilize the number of exposed active sites in strong alkaline environments. Meanwhile, NCQDs with tiny lateral size and abundant functional groups deposited on the surface of the Ni-Fe-S hollow nanostructure and/or into the cavity not only maintain the structural integrity and stability, but also protect the Fe/Ni-based active species in the NiS/FeS nanocage from rapid corrosion. Benefiting from the special structure and the synergistic effect between NCQDs and NiS/FeS, the catalyst (Ni-Fe-S/NCQDs) is expected to exhibit higher activity and durability than commercial Pt/C (ORR) and RuO₂

(OER) in alkaline electrolyte (0.1 M KOH). This study identifies a feasible strategy for optimizing the oxygen electrocatalytic activity of NCQDs-modified transition metal-based sulfides with complex structures by understanding the intrinsic electrocatalytic activity.

2. Experimental section

2.1. Synthesis of NCQDs

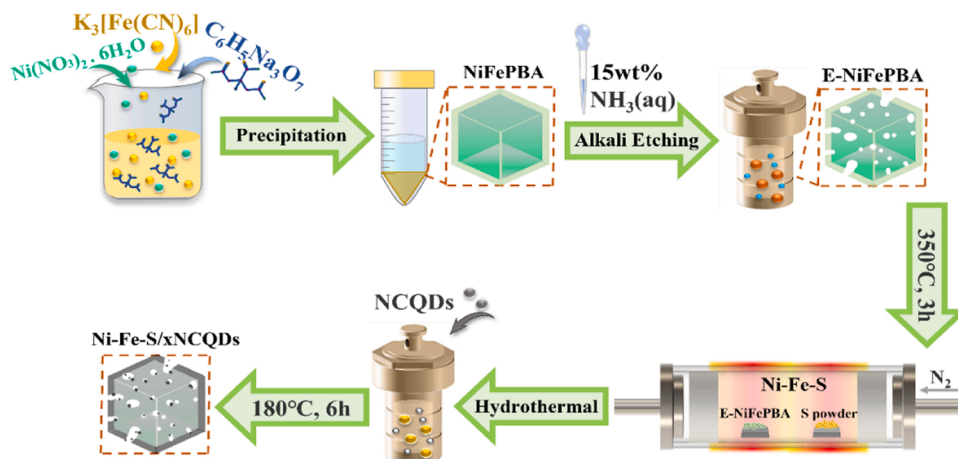
Citric acid monohydrate (CA) (5 g) and urea (2.27 g) were dissolved in 15 mL of deionized water, as carbon and nitrogen sources, respectively. The prepared solution was transferred to a Teflon-lined stainless-steel autoclave and heated at 180 °C for 6 h. After the autoclave was cooled to room temperature (25 °C), the resulting NCQD was centrifuged at 8000 rpm for 50 min to remove any precipitate. Then, the light brown supernatant was dialyzed using a 6–8 kD molecular weight cut-off (MWCO) membrane for 16 h. The resulting solution was dried by using freeze drying at – 50 °C for 16 h in a vacuum drier to obtain the black NCQDs.

2.2. Synthesis of NiFePBA and E-NiFePBA nanocages

In a typical synthetic procedure, 0.30 g of Ni (NO₃)₂·6 H₂O and 0.441 g of trisodium citrate dihydrate were dissolved in 40 mL of deionized (DI) water to form solution A [33]. 0.264 g of K₃[Fe(CN)₆] was dissolved in 60 mL of DI water to form solution B. Then, solution B was quickly added to solution A and stirred for 60 s under magnetic stirring. The obtained mixed solution was aged at room temperature (25 °C) for 24 h, and the precipitate was collected by centrifugation. The precipitate was dried at 70 °C overnight to obtain the NiFePBA nanocubes. The as-prepared NiFePBA nanocubes (0.15 g) and 9 mL of NH₃·H₂O (15 wt%) were mixed in an autoclave with a polytetrafluoroethylene lining pipe and heated in an oven at 160 °C for 3 h to obtain the etched PBA (E-NiFePBA) nanocages.

2.3. Synthesis of Ni-Fe-S nanocages and Ni-Fe-S/xNCQDs

In a typical synthesis process, 10 mg of E-NiFePBA nanocage and 20 mg of S powder were put at two separate positions in a porcelain boat with S powder at the upstream side of the tube furnace. Then, the sample was annealed at 350 °C for 3 h at a heating rate of 2 °C min^{–1} under a nitrogen atmosphere. The Ni-Fe-S nanocages were obtained after cooling to ambient temperature in a nitrogen atmosphere. The Ni-Fe-S/xNCQDs catalysts were prepared by using the self-assembly route (x = 1, 2, 3, 4 and 5). The above NCQDs was dispersed in 17 mL of ethanol and mixed with the Ni-Fe-S nanocages at a weight ratio of 10, 20, 30, 40 and 50 (accordingly, x = 1, 2, 3, 4 and 5) by ultrasonic vibration. Then, the mixture was poured into an autoclave and heated in an oven at 180 °C for 6 h. After that, it was washed with deionized water for five times and kept in a vacuum drying oven at 80 °C for 6 h. The schematic synthesis process was shown in Scheme 1. Commercial Pt/C and RuO₂ were used as the reference catalysts for ORR and OER in this study. Material characterizations including X-ray diffraction (XRD), X-ray photoelectron spectroscopy (XPS), Raman, scanning electron microscopy (SEM), transmission electron microscopy (TEM) and elemental mapping image (EDS), Fourier transform infrared spectroscopy (FT-IR), contact angles and N₂ adsorption/desorption isotherms were introduced in the ‘Supporting Information’. Electrochemical tests including cyclic voltammetry (CV), linear sweep voltammetry (LSV), electrochemical impedance spectroscopy (EIS), rotary disk electrode (RDE), rotary ring disk electrode (RRDE), chronogalvanometry (CA) and accelerated durability test (ADT) were also introduced in the ‘Supporting Information’.



Scheme 1. Synthesis route for Ni-Fe-S/xNCQDs composites.

3. Results and discussion

3.1. Structure and comp

Fig. 1a shows the XRD patterns of NCQDs, NiFePBA and Ni-Fe-S/3NCQDs. The XRD pattern of NiFePBA is completely consistent with that of $\text{K}_3\text{NiFe}(\text{CN})_6$ (JCPDS 51-1897). The peaks at around 18.4° (1 1 0), 30.3° (1 0 1), 35.7° (0 2 1), 37.3° (2 2 0), 50.1° (4 1 0), 57.4° (3 3 0) and 75.6° (0 4 2) match well with the characteristic diffraction peaks of NiS crystal (JCPDS 12-0041), while the diffraction peaks at around 29.9° (1 1 0), 35.5° (2 0 1), 43.1° (1 1 4), 53.7° (3 0 1) and 63.2° (0 0 8) are assigned to the hexagonal FeS crystal phase (JCPDS 37-0477). Due to the similar electronic structure of FeS and NiS, some characteristic peaks of FeS coincide with those of NiS [34]. The diffraction peak at around 44.3° matches with the (3 0 0) plane of sulfur (JCPDS 52-1035), which should originate from the deposited S element (un-reacted) during the vulcanization process. These results indicate that the FeS and NiS phases are successfully formed by vulcanizing NiFe PBA in S vapor. Moreover, the obvious bulge in the XRD pattern of Ni-Fe-S/3NCQDs at around 26.38° corresponds to the diffraction signal of the (0 0 2) plane of graphitized carbon in NCQDs (Fig. 1a), proving the successful incorporation of NCQDs to the Ni-Fe-S nanocages. Fig. 1b shows the XRD patterns of the synthesized Ni-Fe-S/xNCQDs catalysts. Obviously, these XRD patterns are consistent with that of Ni-Fe-S/3NCQDs observed in Fig. 1a. Therefore, the combination of Ni-Fe-S nanocages and NCQDs is

successfully achieved by using the hydrothermal reaction.

XPS tests are used to determine the elemental surface composition and chemical state of NiS/FeS hybrids. Percentage contents of the deconvoluted components of S 2p, C 1s, N 1s, Ni 2p and Fe 2p are shown in Tables S2-S6, respectively. Obviously, S (around 162.0 eV), C (around 284.6 eV), N (around 399.9 eV), Fe (around 712.6 eV) and Ni (around 856.7 eV) atoms are detected on the surface of Ni-Fe-S/3NCQDs (Fig. 2a and Table S1). As shown in Fig. 2b and Fig. S1a, the S 2p_{3/2} and S 2p_{1/2} peaks are located at around 162.01 and 164.02 eV, respectively, which correspond to the typical metal-sulfur bond (M-S) in FeS and NiS. As reported previously, the metal-sulfur bond in metal sulfides has strong covalent property [35], which is beneficial to appropriately adjust the energy band of metal conduction/valence band edge during the oxidation/reduction reaction, implying that the electrochemically active sites for ORR/OER are abundant. The broad peaks at around 168.82 and 169.96 eV are ascribed to the characteristic peaks of the S-O vibration, indicating that there is a certain degree of oxidation on the surface of metal sulfide [36]. The deconvolution plots of C 1s are shown in the Fig. 2c and Fig. S1b. The peaks centered at around 284.6, 285.3, 287.2, and 289.2 eV are assigned to C-C sp₂, C-C sp₃, C-N, and C=N/C=O, respectively. The presence of carbon-oxygen double bond (C=O) implies that the NCQDs with O-containing groups can conduce the absorption and transformation of intermediates on the catalytic surface/active sites in alkaline conditions [37].

The high-resolution N 1s XPS spectrum (Fig. 2d) of Ni-Fe-S/3NCQDs

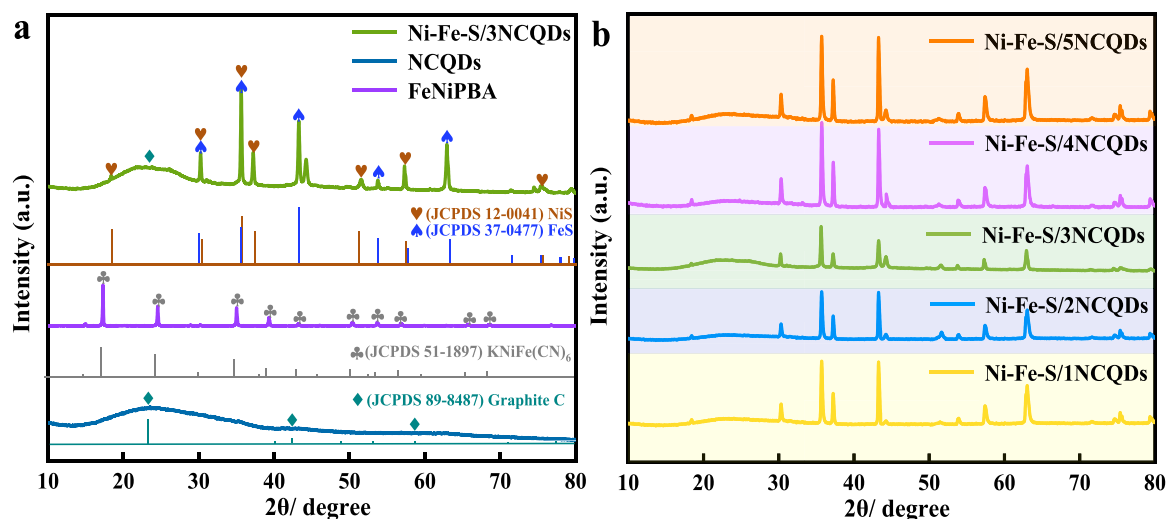


Fig. 1. XRD patterns of NCQDs, NiFePBA and Ni-Fe-S/3NCQDs (a); XRD patterns of Ni-Fe-S/xNCQDs (b).

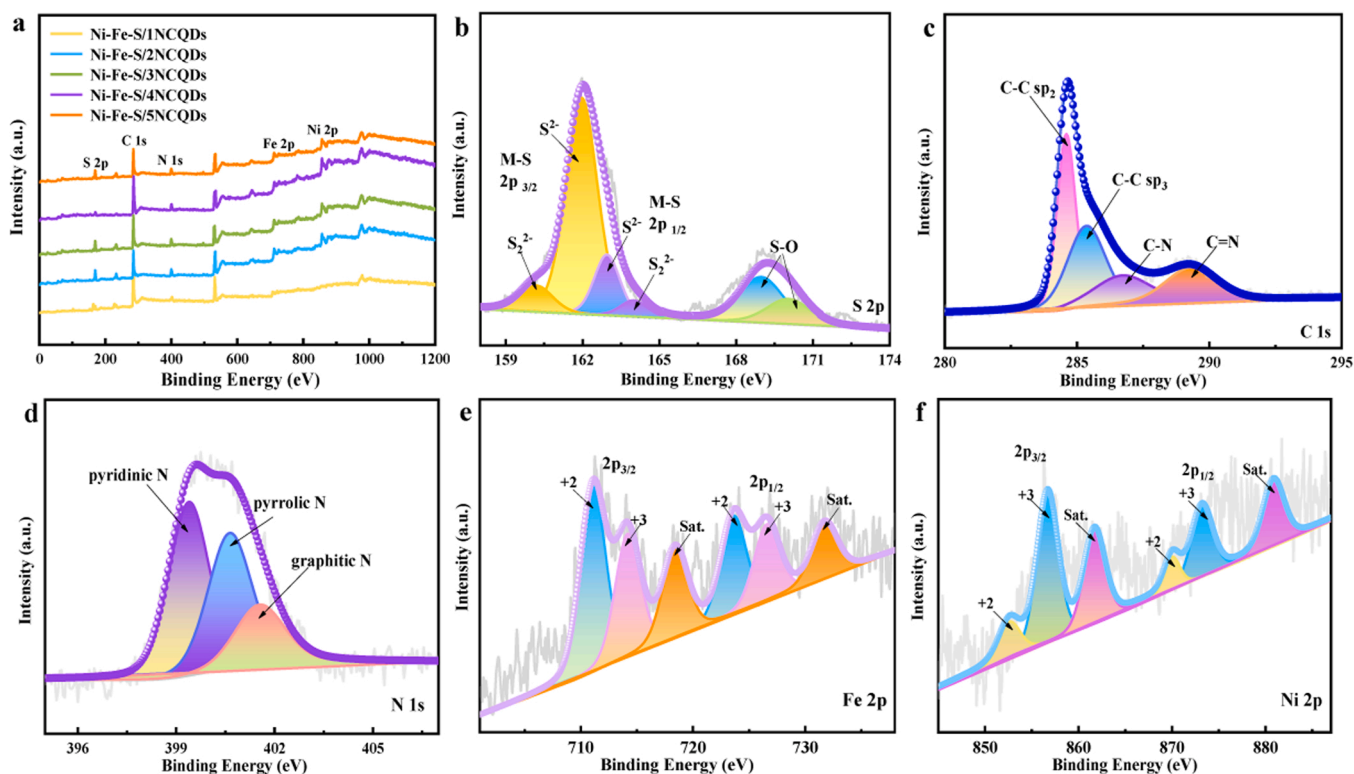


Fig. 2. XPS survey spectra for Ni-Fe-S/xNCQDs (a) and high resolution XPS spectra of S 2p (b), C 1s (c), N 1s (d), Fe 2p (e) and Ni 2p (f) for Ni-Fe-S/3NCQDs.

shows that the pyridine (around 398.4 eV), pyrrole (around 399.94 eV) and graphite N (around 401.72 eV) are existed. It has been demonstrated that the electrocatalytic activity of N-containing catalysts is highly dependent on the pyridine N content, while graphite N can attract electrons from adjacent C atoms to improve oxygen adsorption on the carbon structure. Thus, it is deemed that the high proportion of pyridine N (43.0 %, Table S4) in the Ni-Fe-S/3NCQDs helps to enhance ORR activity. The Fe 2p peaks of Ni-Fe-S/3NCQDs at around 711.1–723.7 eV (Fig. 2e) corresponding to lower (Fe 2p_{3/2}) and higher (Fe 2p_{1/2}) energies due to spin-orbital splitting are also observed. Note that the Fe 2p_{1/2} and Fe 2p_{3/2} peaks of Ni-Fe-S/3NCQDs are located at lower binding energies than some reported values [33]. The negative shift in the binding energy of Fe 2p indicates that the electronic structure of Fe is affected by the coordination effect during the sulfuration process, confirming the existence of FeS in Ni-Fe-S/3NCQDs. As displayed in Fig. 2f and Fig. S1e, the high-resolution XPS spectra of Ni 2p shows the peaks of Ni 2p_{3/2} and Ni 2p_{1/2} at around 856.69 and 873.19 eV accompanied by their satellite peaks at around 861.69 and 880.86 eV, respectively, suggesting that Ni atoms are existed in the Ni (II) state (NiS). In addition, a small positive shift of binding energy for Ni 2p_{2/3} (856.69 vs 855.8 eV) than that of the reported NiS-based catalyst is found [38], indicating that the incorporation of Fe atom can significantly modulate the electronic structure of Ni center.

The Raman spectra of Ni-Fe-S/NCQDs and NCQDs catalysts are shown in Fig. 3a, where the D band at around 1274 cm⁻¹ and the G band at around 1455 cm⁻¹ are attributed to the structural defects on the graphite plane and the E_{2g} vibration mode corresponding to the sp₂ bonded graphite carbon, respectively. The intensity ratio of D-band and G-band (I_D/I_G) reveals the degree of graphitization [23,39]. Obviously, Ni-Fe-S/3NCQDs catalyst exhibits a higher G band intensity and a lower value of I_D/I_G than those of NCQDs, implying that it has a higher graphitization degree. Generally, a higher graphitization degree contributes to a better electrical conductivity of the carbon skeleton [39]. Therefore, Ni-Fe-S/3NCQDs with a higher graphitization degree should facilitate a faster electron transfer. The functional groups on the surface

of Ni-Fe-S/3NCQDs is disclosed by FTIR spectroscopy (Fig. 3b). The two characteristic peaks of Ni-Fe-S/3NCQDs at around 1217 and 1610 cm⁻¹ correspond to C-C and C=C, respectively, which are consistent with those of NCQDs. Moreover, the ν (NH) peak for NH₄⁺ at around 1416 cm⁻¹ and the ν (CN) peak at around 2091 cm⁻¹ in the FTIR spectra indicate that the redox reaction may be involved in the etching process (Eq. S1) [33]. The broad peak at around 3228.2 cm⁻¹ should correspond to the hydrogen-bonded hydroxyl group from the hydroxide layer and/or the interlayer water [33].

N₂ adsorption and desorption tests are performed for Ni-Fe-S/3NCQDs and the specific surface area (SSA) and pore structure are shown in Fig. 3c. The mesoporous property of Ni-Fe-S/3NCQDs catalyst is confirmed by the typical IV hysteric loop, which is consistent with the pore size distribution curve. As displayed in Table S7 and Fig. S2 (Supporting Information), the SSA values of NCQDs, NiFePBA, E-NiFePBA, Ni-Fe-S and Ni-Fe-S/3NCQDs are 21.561, 216.25, 518.21, 482.16 and 478.35 m² g⁻¹, respectively. It is speculated that the large SSA and abundant mesoporous structure originate from the holes and cavities created during the process of cube-to-cage conversion by chemical ammonia etching [40–42]. These abundant mesopores and hollow shells allow the gathering of oxygen to fully utilize the exposed active sites [33,41]. The porous structure provides smooth pathways for the rapid mass transfer, which facilitates the adsorption, conversion and desorption of the oxygen-related reactants/intermediates produced in the catalytic process to improve the ORR/OER efficiency [42,43]. The contact angle is used to evaluate the wettability of the liquid electrolyte solution to the solid catalyst, and a smaller angle value means that the active sites in the catalyst can easily contact with the electrolyte solution [40]. The contact angles of Ni-Fe-S/3NCQDs and FeNiPBA are shown in Fig. 3d and Fig. S3, respectively. The contact angle of Ni-Fe-S/3NCQDs (17.94°) is much smaller than that of NiFePBA (36.50°) due to the rough surface from the multi-cavities. The highly hydrophilic surface can reduce the O₂ and OH⁻ ion mass transfer resistance and promote the kinetic and/or mass transport processes at the electrode-electrolyte interface [43,44]. In addition, as shown in Fig. S3, the hydrophilicities

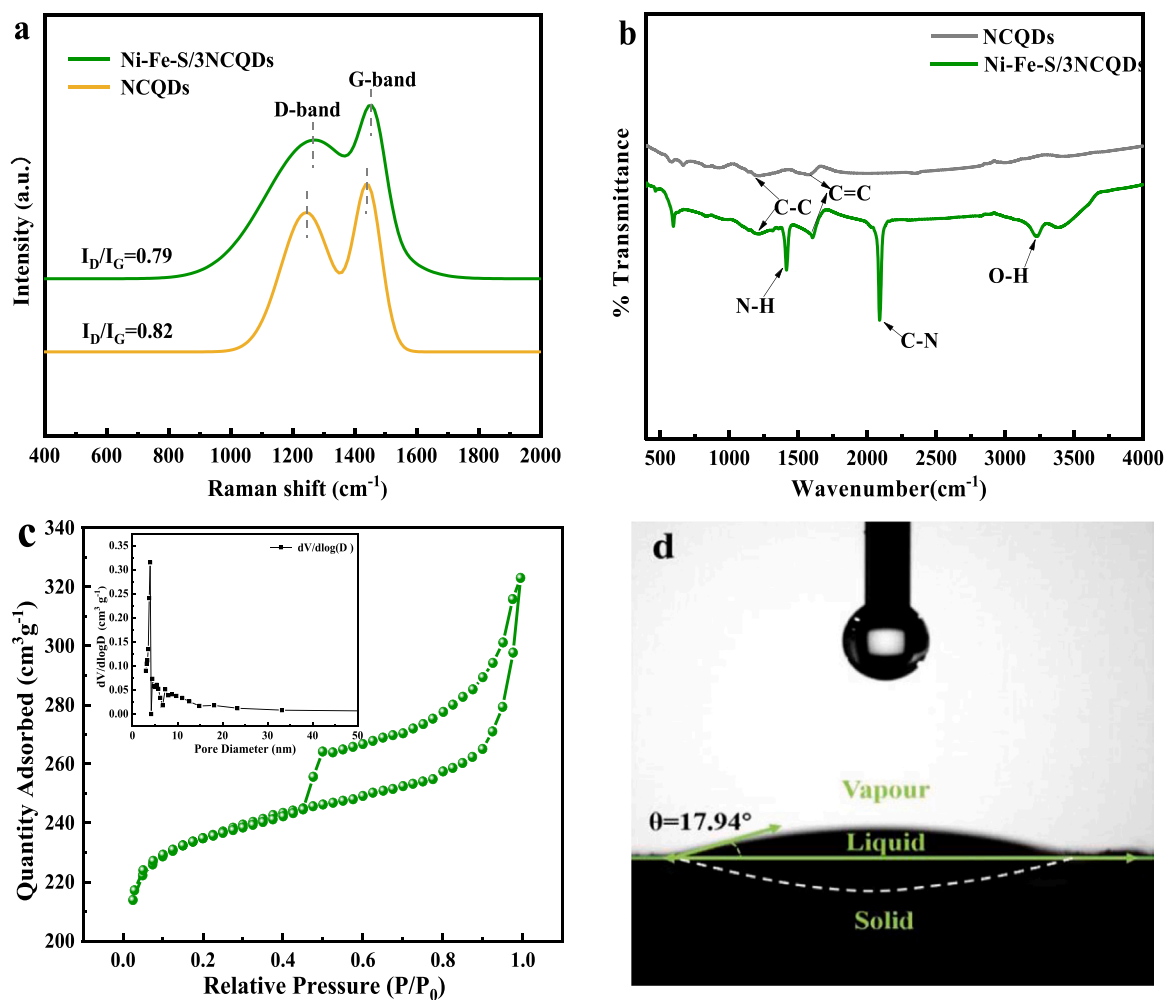


Fig. 3. Raman spectra of NCQDs and Ni-Fe-S/3NCQDs (a); FT-IR patterns of NCQDs (b) and Ni-Fe-S/3NCQDs; N_2 adsorption/desorption isotherms (c) and pore size distributions (inset) for Ni-Fe-S/3NCQDs and Contact angles of Ni-Fe-S/3NCQDs (d).

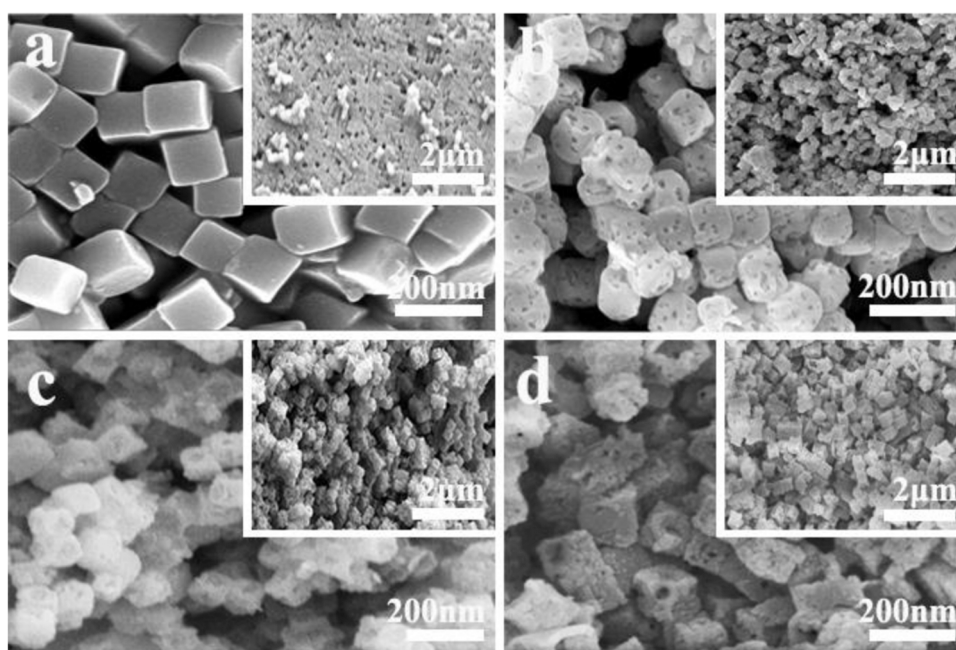


Fig. 4. SEM images of NiFePBA (a), E-NiFePBA (b), Ni-Fe-S (c), and Ni-Fe-S/3NCQDs (d).

of Ni-Fe-S/NCQDs catalysts change significantly with the occurrence of etching by comparing with NiFePBA, E-NiFePBA and Ni-Fe-S. Other Ni-Fe-S/NCQDs catalysts also have high surface hydrophilicities, and the contact angle changes significantly with the increase of the NCQDs loading, which is mainly due to the change in the number of interconnected pore channels [45,46].

Fig. 4 shows the SEM images of NiFePBA, E-NiFePBA, Ni-Fe-S and Ni-Fe-S/3NCQDs. The smooth surface and clear contour of the architecture (NiFePBA) are shown in Fig. 4a, and a wider field of view observed in the inset shows the uniform distribution of the NiFePBA cubes. Some studies have shown that isotropic alkaline etching can convert solid nanocubes into hollow nanocages [33,47]. As shown in Fig. 4b, E-NiFePBA with multiple holes on the outer surface is prepared by adjusting the content of ammonia. The average size of E-NiFePBA is approximately 120 nm, which well inherits the morphology and size of the nanocube template. Fig. 4c shows that after the sulfuration of the precursor, the skeleton of the porous hollow cage (Ni-Fe-S) has slightly shrunk at the high temperature. In Fig. 4d, the unique hollow internal cavities can be directly seen through the fractured nanocage and the porous channels are well retained on the surface of the catalyst, suggesting the formation of an open structure of the nanocages. Note that small-sized NCQDs are not easily observed by SEM, however, the rougher surface is clearly displayed. The well-designed internal voids and hollow configurations should possess large surface areas, which are consistent with the SSA results and grant the ready accessibility of active sites and good wettability by electrolyte. It facilitates the full utilization of the catalyst to promote reaction kinetics and cycling lifespan.

The shape and structure of the hollow inner space of the porous nanocage are further studied by TEM (Figs. 5a-j). The dispersed N-doped CQDs (NCQDs) with a size of 5–10 nm can be clearly display in Fig. 5a, and Fig. 5b shows a highly uniform nanocage with an average particle diameter of approximate 150 nm, which is consistent with the SEM

results. The E-NiFePBA with a hollow structure and a highly porous surface is obtained by etching NiFePBA cubes with alkali (Fig. 5c), while the sulfuration does not influence this unique structural feature (Fig. 5d). The etching increases the number of holes and the specific surface area of the catalyst, which further facilitates the effective diffusion of the electrolyte and the exposure of more active sites [3,48]. In addition, it is known that the S atom with a low electronegativity can be covalently bonded to the metal ions to change the energy band structure of transition metals, lower the redox potentials of metals, and enhance conductivity, which correspondingly improve the catalytic activity of Ni-Fe-S/xNCQDs [8,48].

In Figs. 5e–5i, the small-sized NCQDs is anchored in the porous framework of Ni-Fe-S through hydrothermal technology (NCQD is marked by a red circle in Fig. 5e). With the increase of NCQDs content, the internal space of Ni-Fe-S/xNCQDs ($x = 1, 2, 3, 4$ and 5) is gradually filled and the pores in skeleton are also blocked. Excessive addition of NCQDs may cause the accessible space to be occupied to lose the mass transfer pathways, thereby reducing the electrocatalytic activity [43, 46]. The connection interface between multiple components can effectively adjust the redox reactivity of metal sites, accelerate the electron transfer rate and promote the occurrence of synergistic effects in the electrocatalytic process [49,50]. In Fig. 5j, NCQDs are distributed on the edge and inside of Ni-Fe-S/3NCQDs. The high-resolution TEM (HRTEM, Figs. 5k and 5l) images show that a clear lattice fringe is observed at the two-phase interface with an interplanar distance of 0.343 nm, which can be ascribed to the (0 0 2) planes of graphitic carbon. It indicates that NCQDs are successfully doped into the porous hollow cage and loaded on the surface. The marked square areas in Fig. 5l shows the corresponding HRTEM images (Fig. 5m and n), verifying the successful synthesis of NCQDs, NiS and FeS in the porous cube of Ni-Fe-S/3NCQDs. As shown in Fig. 5m, the lattice spacing of 0.251 nm corresponds to the (0 2 1) crystal plane of NiS, while the lattice spacing of 0.246 nm

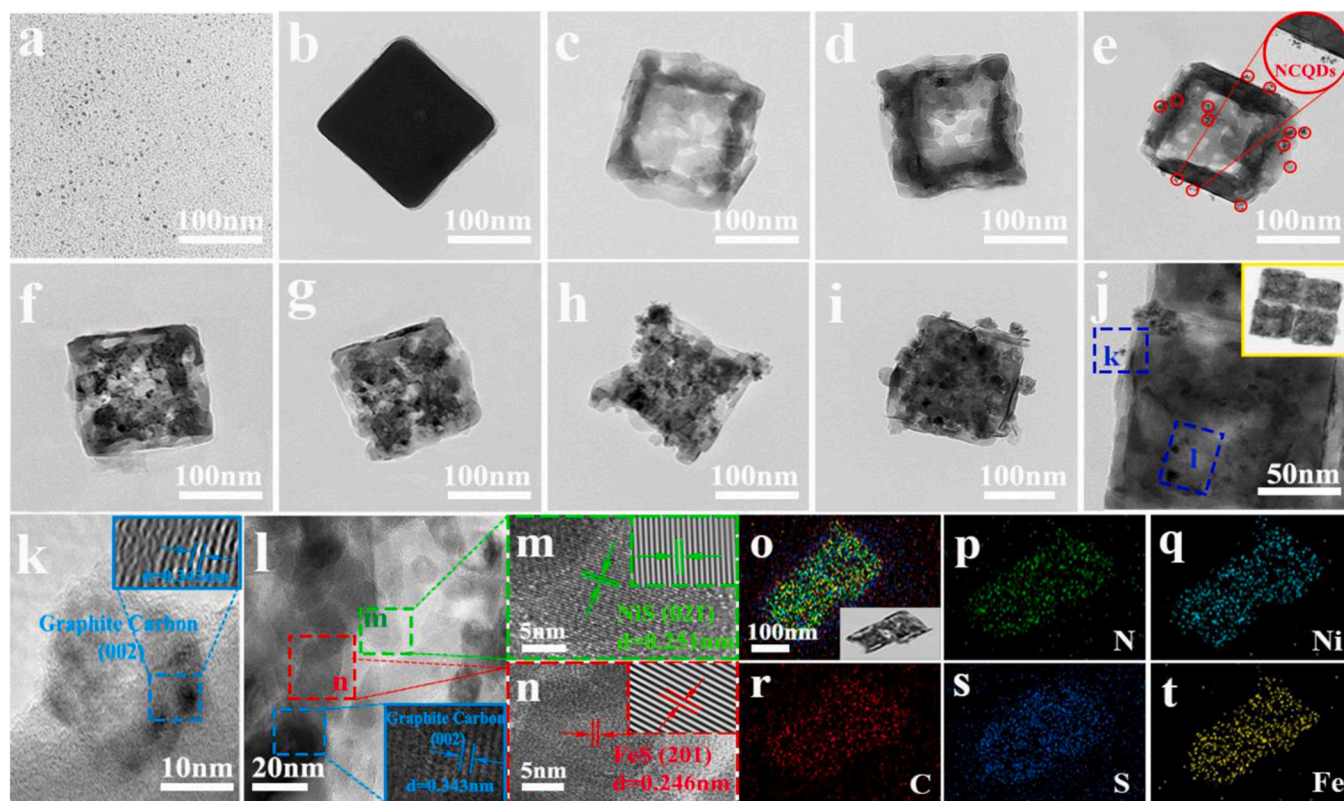


Fig. 5. TEM images of NCQDs (a), NiFePBA (b), E-NiFePBA (c), Ni-Fe-S (d) and Ni-Fe-S/xNCQDs ($x = 1$ (e), 2 (f), 3 (g), 4 (h) and 5 (i)); TEM images of Ni-Fe-S/xNCQDs (j); HRTEM images of Ni-Fe-S/xNCQDs (k and l correspond to the square regions marked in TEM image (j)); (m) and (n) correspond to the square regions marked in HRTEM image (l); Elemental mapping images of the mixed elements (o), N (p), Ni (q), C (r), S (s), and Fe (t).

corresponds to the (2 0 1) crystal plane of FeS in Fig. 5n. In Fig. 5o-t, the elemental mapping images confirms the co-existence of Ni, Fe, S, C and N elements, which further confirms that the NCQDs are successfully introduced to the framework (surface) of Ni-Fe-S.

3.2. Electrocatalytic activities of Ni-Fe-S/xNCQDs catalysts for ORR

The ORR activities of NCQDs, NiFePBA, E-NiFePBA, Ni-Fe-S, Ni-Fe-S/3NCQDs and commercial Pt/C are evaluated by using CV tests under alkaline conditions. Among all the prepared catalysts, the Ni-Fe-S/3NCQDs shows the most promising ORR activity, and the reduction peak is located at 0.851 V, which is slightly better than that of 10 wt% Pt/C (0.837 V), as shown in Fig. 6a. The reduction peaks of reference samples are also shown in Fig. 6a. It is evident that the great improvement in ORR activity of Ni-Fe-S is acquired after the incorporation of NCQDs, which is ascribed to the intrinsic electronic properties of NCQDs originating from the conjugation between carbon π -system and nitrogen lone pair electrons [51,52]. Moreover, NCQDs in the porous structure increases the contact probability of the reactants with the catalytic active sites to enhance the adsorption capacity for intermediates, thereby accelerating the ORR rate [53]. In Fig. 6b, the reduction peaks of Ni-Fe-S/xNCQDs ($x = 1, 2, 4$ and 5) are located at around 0.737, 0.772, 0.805 and 0.788 V, respectively. The differences in the reduction peaks of Ni-Fe-S/xNCQDs catalysts indicate that the effectual synergies between Ni-Fe-S and NCQDs are obtained in the special structure. The LSV (Fig. 6c) curve of Ni-Fe-S/3NCQDs shows an onset potential (E_{onset}) of 0.97 V and a half-wave potential ($E_{1/2}$) of 0.85 V (The current densities used for the determination of E_{onset} and j_L are -0.20 and

-2.06 mA cm^{-2} , respectively), which are more positive than those of Pt/C ($E_{\text{onset}}=0.95 \text{ V}$ and $E_{1/2}=0.841 \text{ V}$) and other Ni-Fe-S/xNCQDs catalysts (Fig. 6d), and recently-reported catalysts (Table S8), indicating that Ni-Fe-S/3NCQDs has a better catalytic activity. It is noted that the decrease in ORR activities of Ni-Fe-S/4NCQDs and Ni-Fe-S/5NCQDs may be attributed to the clogging of the pores on the catalyst structure by excessive NCQDs to tremendously impede the mass transfer. In addition, the ORR performances of Ni-Fe-S/3NCQDs, NiS/3NCQDs and FeS/3NCQDs are recorded in Fig. S4. The activity enhancement should be attributed to the synergies between FeS and NiS induced by metal neighbours, which facilitates the adsorption of intermediates during ORR [54,55].

Tafel slope is suitable to evaluate the efficiency of electrocatalysts in increasing current density at the expense of overpotential. A lower Tafel slope is expected to achieve a high current density at a low overpotential, implying that the catalyst has a faster ORR kinetics [40]. The Tafel slope of Ni-Fe-S/3NCQD ($78.01 \text{ mV dec}^{-1}$) obtained in Fig. 6e is smaller than that of Pt/C ($126.95 \text{ mV dec}^{-1}$), implying that the efficient ORR kinetic of Ni-Fe-S/3NCQDs. This is mainly attributed to the high exposure of accessible active sites have and the short diffusion paths between NiS/FeS and NCQDs for fast mass transfer via the limited space inside the hollow catalyst cage. The main feature of the Nyquist diagram is the half-arc formed at low frequencies, and its radius is a measure of the charge transfer resistance (R_{ct}) at the electrode/electrolyte interface. As shown in Fig. 6f and Fig. S5, the R_{ct} value of Ni-Fe-S/3NCQDs is 15.86Ω , which is much lower than those of Pt/C (29.67Ω) and NCQDs (44.01Ω). The low R_{ct} value of Ni-Fe-S/3NCQDs indicates the faster charge transfer rate, implying that more effective electron transfer

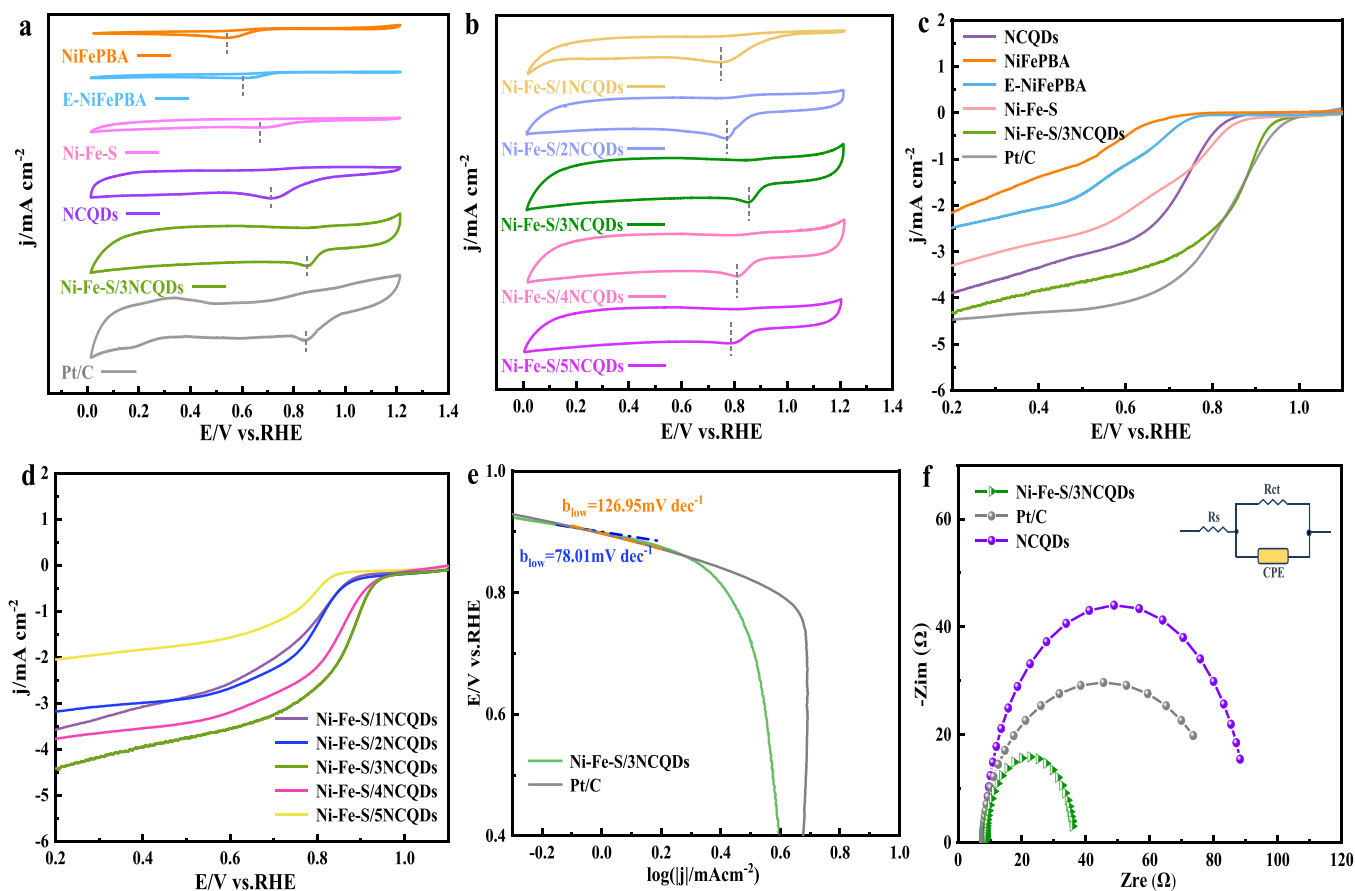


Fig. 6. CV curves for NiFePBA, E-NiFePBA, Ni-Fe-S, NCQDs, Ni-Fe-S/3NCQDs (a) and Pt/C; CV curves for Ni-Fe-S/xNCQDs ($x = 1, 2, 3, 4$ and 5) in an O_2 -saturated 0.1 M KOH solution at 10 mV s^{-1} (b); LSV curves (5 mV s^{-1} and 1600 rpm) for NiFePBA, E-NiFePBA, Ni-Fe-S, NCQDs, Ni-Fe-S/3NCQDs and Pt/C in an O_2 -saturated 0.1 M KOH solution (c); LSV curves for Ni-Fe-S/xNCQDs (d); Tafel plots of the Ni-Fe-S/3NCQDs and Pt/C (e); Nyquist curves of Ni-Fe-S/3NCQDs, NCQDs and Pt/C at an amplitude of 5 mV with a rotation rate of 1600 rpm in an O_2 -saturated 0.1 M KOH solution (f).

kinetics is obtained within the electrode and/or at the electrode/electrolyte interface at higher potentials. It indicates that Ni-Fe-S/3NCQDs has the more efficient ORR process (charge transfer), which is consistent with the Tafel results.

The inset in Fig. 7a shows the linear Koutecky-Levich (K-L) curves (almost overlapped) at different applied potentials, indicating that the dissolved oxygen in the electrolyte follows the first-order reaction kinetics on the Ni-Fe-S/3NCQDs. The number of transferred electrons (n) for Ni-Fe-S/3NCQDs (from 3.97 to 4.03) are very close to those of Pt/C in a wide potential range from 0 to 0.8 V (Figs. 7a, b and S6a). RRDE voltammograms of Pt/C, NCQDs and Ni-Fe-S/3NCQDs are shown in Fig. 7c. The peroxide (H_2O_2) yields on Ni-Fe-S/3NCQDs are strikingly suppressed to less than 3.06 % (Fig. 7d), which is slightly lower than that of Pt/C (from 3.61 % to 3.70 %), suggesting a $4e^-$ ORR pathway and an excellent selectivity for reducing O_2 to OH^- . The electrochemical active surface area (ECSA) is calculated by using the double layer capacitance (C_{dl}) of the catalyst. We also use the ECSA value to evaluate the specific activity (SA) of the catalyst for ORR. In Fig. S6b and S6c, it is found that the SA of Ni-Fe-S/3NCQDs stays around 4.11 mA cm^{-2} in the potential range of 0.96–1.1 V, which is better than those of the recently-reported catalysts [56–60]. As reported previously, Fe^{2+} usually displays an extremely high adsorption affinity toward O_2 and a moderate adsorption affinity toward H_2O [7,61]. Thus, the Ni-Fe-S/xNCQDs can capture O_2 from the electrolyte easily and also release H_2O (OH^-) easily, thereby promoting the ORR reaction kinetics. As reported previously, Ni-species may not be directly participated in the ORR procedure, however, Ni sites can improve the adsorption capacity for reactant gas (O_2) and adsorb the OH^* species more tightly during ORR process [62,63], which may contribute to a cumulative enhancement in ORR activity for

Ni-Fe-S/xNCQDs. Therefore, the cooperation of FeS and NCQDs mainly boost the adsorption and reduction of O_2 to promote the entire ORR process with a high $4e^-$ selectivity.

The catalytic stabilities of Ni-Fe-S/3NCQDs and Pt are evaluated by CA tests (Fig. 7e). After the continuous tests for 30,000 s, the current densities of Ni-Fe-S/3NCQDs and Pt/C decrease by 10.21 % and 30.54 %, respectively. Furthermore, no change in current density can be observed after the addition of methanol to 0.1 M KOH electrolyte, confirming the high methanol tolerance of Ni-Fe-S/3NCQDs (Fig. 7f). These results also confirm the long-term ORR stability of Ni-Fe-S/3NCQDs under alkaline conditions. In Fig. S7a and S7b (ADT), the voltammogram recorded over 5000 cycles only negatively shifts 12.8 mV for Ni-Fe-S/3NCQDs, while Pt/C has a negative shift of 17.2 mV. The metal-sulfur bonds in the catalyst have a strong covalent character, which is beneficial to adjust the conduction band/valence band edge to increase the activity in the electrochemical redox reaction [35,61,64]. Meanwhile, the S component covalently-combined with iron ions in the catalyst can be served as the host lattice to improve conductivity and prevent electrolyte corrosion simultaneously [64,65]. In addition, the porous hollow cage structure of Ni-Fe-S/3NCQDs avoids the dissolution and agglomeration of NCQDs nanoparticles, thereby improving the ORR stability.

3.3. Electrocatalytic activities of Ni-Fe-S/xNCQDs catalysts for OER

Fig. 8a shows the electrocatalytic activities of all Ni-Fe-S/xNCQDs catalysts by using LSV tests without any iR compensation in 0.1 M KOH electrolyte. The Ni-Fe-S/3NCQDs catalyst requires an overpotential of 295.4 mV to reach the current density of 10 mA cm^{-2} ,

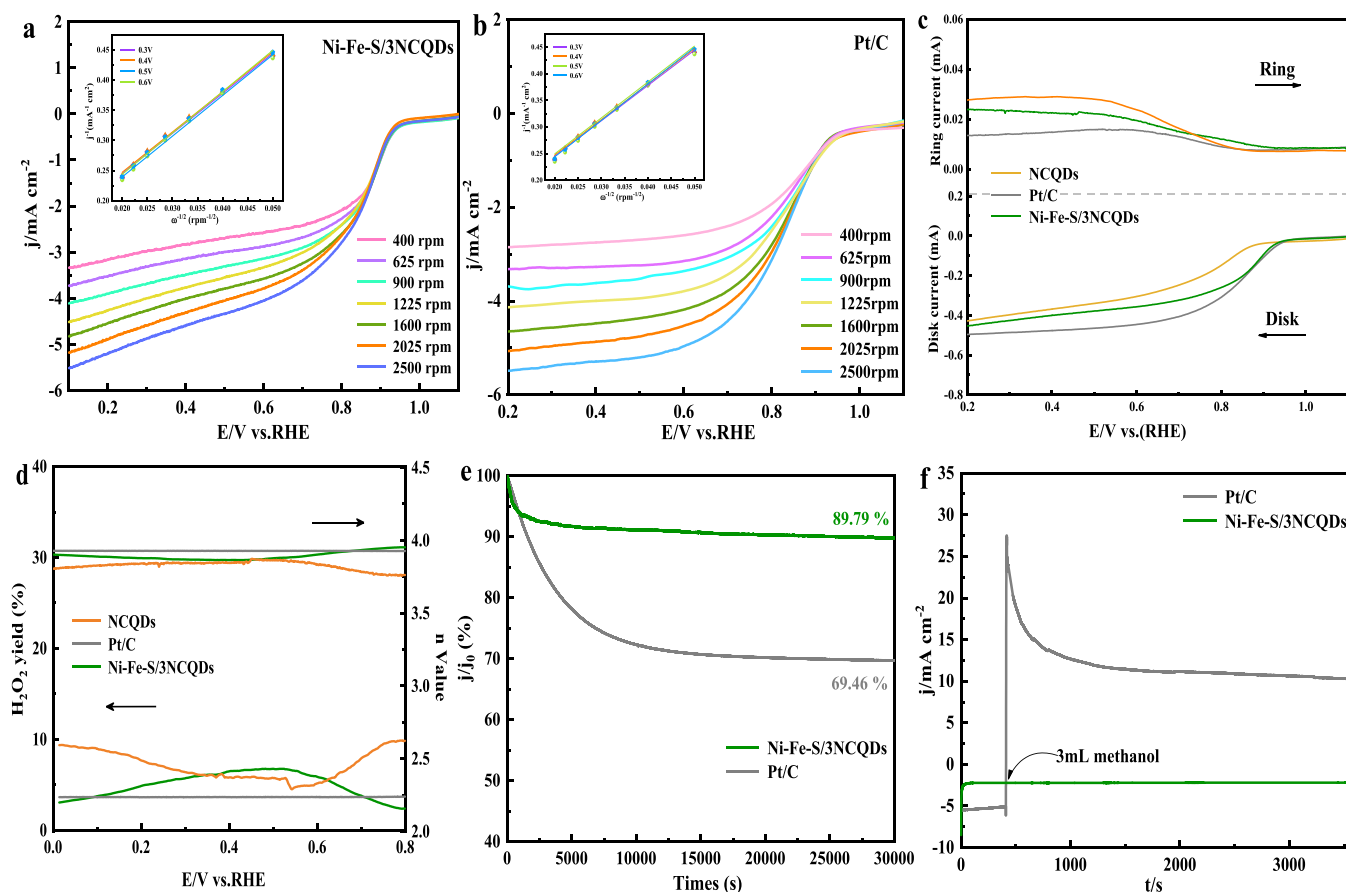


Fig. 7. LSV curves and calculated K-L plots (inset) at different potentials of Ni-Fe-S/3NCQDs (a) and Pt/C (b) in an O_2 -saturated 0.1 M KOH at different RDE rotation rates (5 mV s^{-1}); RRDE voltammograms of Pt/C, NCQDs and Ni-Fe-S/3NCQDs (c); H_2O_2 yields and electron transfer number (n); Chronoamperometric (i-t) responses of Ni-Fe-S/3NCQDs (d) and Pt/C before (e) and after (f) the addition of 3 mL of methanol in an O_2 -saturated 0.1 M KOH at 1600 rpm.

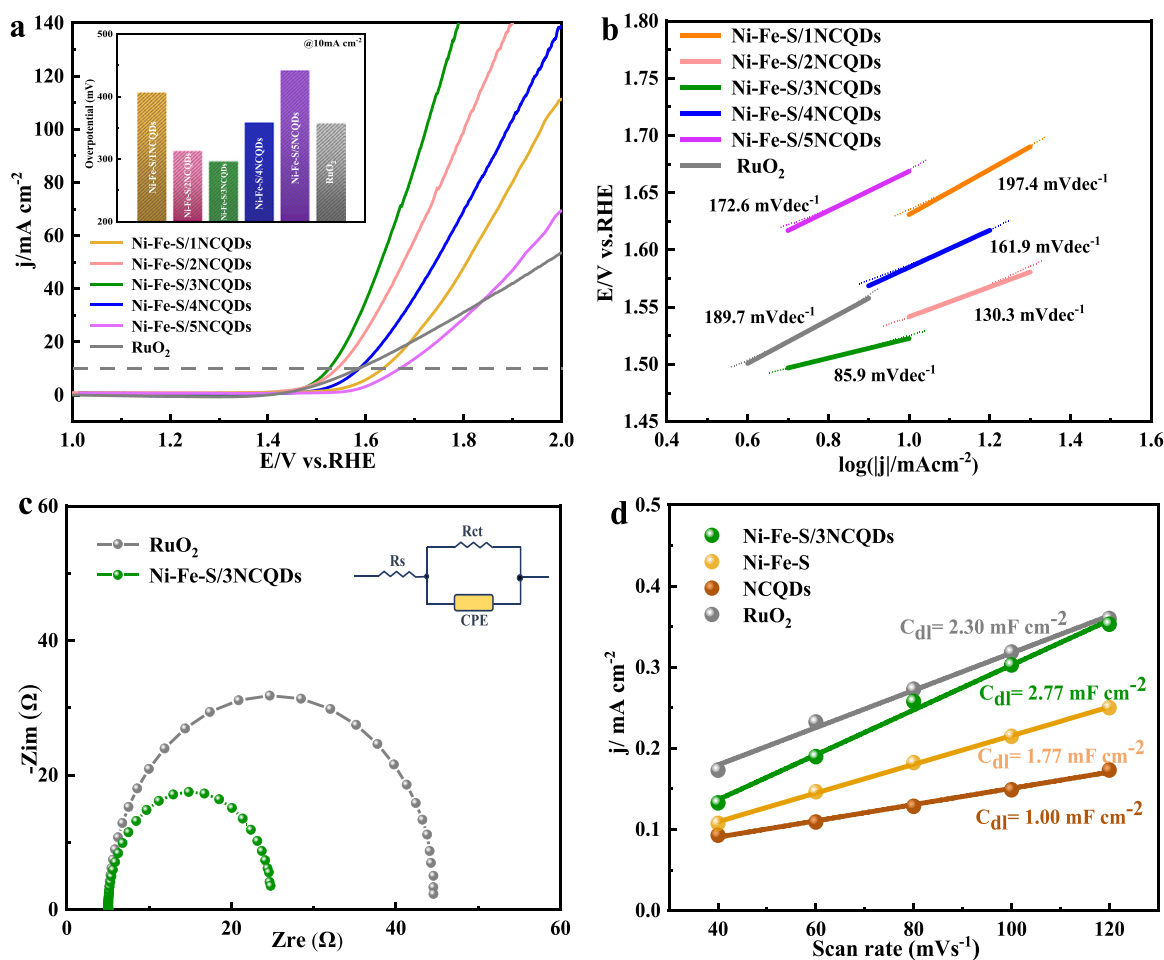


Fig. 8. LSV curves of RuO₂ and Ni-Fe-S/xNCQDs ($x = 1, 2, 3, 4$ and 5) in 0.1 M KOH solution (2 mV s^{-1} and 1600 rpm) for OER (a); Tafel plots of Ni-Fe-S/xNCQDs and RuO₂ (b); Nyquist curves (5 mV s^{-1} and 1600 rpm) of Ni-Fe-S/3NCQDs and RuO₂ (c); Linear plots of scan rates vs. current density for Ni-Fe-S/3NCQDs, NiS/FeS, NCQDs and RuO₂ in 0.1 M KOH electrolyte (d).

which is 60.8 mV lower than that of RuO₂ catalyst (the inset of Fig. 8a). In addition, the current density of the Ni-Fe-S/3NCQDs catalyst can reach 100 mA cm^{-2} with an overpotential of 493.4 mV , while the commercial RuO₂ cannot reach 100 mA cm^{-2} within the applied potential range. The OER performance comparison of Ni-Fe-S/3NCQDs and other recently-reported catalysts are summarized in Table S9. It shows that the lowest overpotential and the fastest rising rate of current density are obtained on Ni-Fe-S/3NCQDs. Generally, Ni/Fe atoms on the catalyst surface are partially oxidized into NiOOH/FeOOH to mainly improve the OER activity. Moreover, the Fe species can exert the partial charge transfer activation effect on Ni species, which affects the binding of oxygenic intermediates [65,66], thereby increasing the OER activity of Ni-Fe-S/3NCQDs (Fig. S8). As shown in the Fig. 8b, the Ni-Fe-S/3NCQDs exhibits enhanced reaction kinetics with the lowest Tafel slope of 85.9 mV dec^{-1} compared with those of Ni-Fe-S/xNCQDs ($x = 1, 2, 4$ and 5) and RuO₂, which is consistent with the fastest current density rise of Ni-Fe-S/3NCQDs in Fig. 8a. The existed $\text{Ni}^{2+}/\text{Fe}^{2+}$ (NiOOH/FeOOH) interface can adjust their local atomic environments to fast the electron transfer and increase the active sites for OER [67–71]. In addition, the strong interactions between NiS/FeS (grown in situ in the nanocage skeleton) and NCQDs (embedded in the nanocage surface/interior) should provide an effective pathway for the electron transport through the entire electrode to obtain the rapid reaction kinetics [72,73].

As shown in Fig. 8c, the Nyquist plot for Ni-Fe-S/3NCQDs obtained at 1.53 V (vs. RHE) reveals a much smaller R_{ct} (17.51Ω) than that of RuO₂

(31.8Ω). In addition, the R_{ct} values of NCQDs and NiS/FeS are 24.4 and 38.57Ω , respectively (Fig. S9). It illustrates that the Ni-Fe-S/3NCQDs catalyst exhibits the most efficient charge transfer process because the in-situ formation of highly-efficient NiOOH/FeOOH species contributes to the accelerated OER activity and reaction kinetics to facilitate the charge transfer on Ni-Fe-S/3NCQDs [74]. The electrochemical active surface area (ECSA) reflects the actual number of active sites exposed on the catalyst to indicate the level of intrinsic activity of the catalyst [43, 46,75]. ECSA is usually evaluated by the double layer capacitance (C_{dl}) because it is assumed to be linearly proportional to the C_{dl} of the catalyst. In Fig. 8d, the Ni-Fe-S/3NCQDs catalyst exhibits a higher value of C_{dl} (2.77 mF cm^{-2}) than those of NiFePBA (1.77 mF cm^{-2}), NCQDs (1.0 mF cm^{-2}) and RuO₂ (2.3 mF cm^{-2}). Accordingly, the ECSAs of Ni-Fe-S/3NCQDs, NiFePBA, NCQDs and RuO₂ are 69.25 , 44.25 , 25 and 57.5 cm^2 , respectively. The largest ECSA of Ni-Fe-S/3NCQDs is chiefly attributed to the unique structure of the small-sized NCQDs embedded in the porous skeleton of hollow nanocage to promote the electrolyte diffusion and O₂ release. The porous carbon thin-wall can expose sufficient OH⁻-adsorption sites and electrocatalytically active sites, while the coated NCQDs can avoid the corrosion of Ni/Fe-oxhydroxides (in situ generated) during OER. The TOF value reflects the relationship between the number of active sites and the catalytic reaction rate calculated from the redox characteristics (CV) area (Fig. S11). Significantly, the calculated mass activity is as high as 8403 A g^{-1} at an overpotential of 295.4 mV and the corresponding TOF reaches 0.722 s^{-1} , which are higher than those of RuO₂ (4680 A g^{-1} and

0.2958 s^{-1}), confirming that Ni-Fe-S/3NCQDs has an excellent intrinsic OER activity.

The FE of Ni-Fe-S/3NCQDs is obtained by the RRDE test, which involves the $4\text{OH}^- \rightarrow 2\text{H}_2\text{O} + \text{O}_2 + 4\text{e}^-$ process. As shown in Fig. 9a and inset, it confirms the effective 4e^- transfer pathway for OER. In addition, when 0.1823 mA is applied to the disk electrode to generate O_2 , the detected ring current is 0.0783 mA and the calculated Faradaic efficiency is 93.68 % (Fig. 9b). The OER stability of the Ni-Fe-S/3NCQDs catalyst is evaluated by successive CV scanning for 1000 cycles. The $E_{j=10}$ of Ni-Fe-S/3NCQDs only increases 17 mV (Fig. 9c) in the potential range of 1.0–2.0 V (vs. RHE). In addition, the chronoamperometry is also used to evaluate the current density of the catalyst to further verify the OER stability of Ni-Fe-S/3NCQDs (the inset of Fig. 9c). It shows a slight change (decrease of 7.05 %) of current density after continuous operation for 20 h, indicating an excellent electrochemical stability of Ni-Fe-S/3NCQDs in long-term operation for OER. The excellent OER activity and stability are attributable to the presence of sulfides in Ni-Fe-S/3NCQDs, which are popular to adsorb OH^- on the surface of Ni-Fe-S/3NCQDs and promote more Ni/FeOOH active phases formed during the oxidation process [76,77]. The active sites (NiOOH/FeOOH) on the internal/external surfaces can fully ensure the electrocatalytic stability during the long-term operation [76]. Note that the internal in-situ growth of the active species may enhance OER activity by space confinement effect in the special hollow cage, i.e., the porous wall restricts the leaching of active substances and promotes mass transfer, thereby facilitating to the long cycling life of OER in alkaline media. These merits further facilitate the high charge transfer rate at the gas/electrode/electrolyte three-phase boundary to synergistically boost the oxygen evolution on Ni-Fe-S/3NCQDs [31,33,66].

To investigate the component change and the actual active sites of the catalyst after the long-term OER tests, the in-situ XRD tests are conducted to explore the intermediates on Ni-Fe-S/3NCQDs during OER. The diagram for in-situ XRD equipment is shown in Fig. 10a. New diffraction peaks are found at around 25.95° , 37.93° and 48.37° during OER, which are indexed to the (0 0 6), (1 0 2) and (1 0 7) lattice planes of NiOOH (JCPDS No. 06–0075), respectively (Fig. 10b). The highly oxidized nickel species are widely believed to be existed in the form of NiOOH, which has a more disordered structure and can provide a higher OER activity [43,66]. In addition, the peaks at around 47.13° , 66.09° and 68.69° correspond to the (0 5 1), (2 6 0) and (2 5 1) lattice planes of γ -FeOOH (JCPDS No. 76–2301), respectively (Fig. 10b). It indicates that the Fe^{2+} in Ni-Fe-S/3NCQDs is oxidized to Fe^{3+} at higher potentials to form the Fe oxyhydroxide (γ -FeOOH), which improves the adsorption and oxidation capacity of water molecules at Fe sites [74]. The high resolution XPS spectra are shown in Fig. 10c, and the positive shifts of the binding energies of the Fe $2p_{3/2}$ and Fe $2p_{1/2}$ core levels can be

clearly observed after OER test (Fig. 10d), indicating the oxidation of the Fe (II) species in Ni-Fe-S/3NCQDs. The XPS peaks at around 713.1 eV and 726.3 eV correspond to Fe^{3+} (from FeOOH) in Fe $2p_{3/2}$ and Fe $2p_{1/2}$, respectively. As shown in the XPS spectra of Ni species after OER (Fig. 10e), Ni $2p_{3/2}$ and Ni $2p_{1/2}$ are located at around 855.2 and 872.8 eV, respectively. The increased $\text{Ni}^{3+}/\text{Ni}^{2+}$ ratios clearly indicate that Ni^{2+} is oxidized to Ni^{3+} with the formation of Ni oxyhydroxide (NiOOH) as the most active species for OER. As pointed by literatures, it should be noted that the cooperation between FeOOH and NiOOH (with the possible formation of $\text{Ni}_{1-x}\text{Fe}_x\text{OOH}$) should possess a far higher catalytic activity than NiOOH alone for OER [38,67,68,73]. Moreover, the O 1s XPS spectrum of Ni-Fe-S/3NCQDs exhibits more M-O and M-OH bond content (Fig. 10f), confirming that more oxyhydroxides are formed in Ni-Fe-S/3NCQDs. The peak at around 533.4 eV should correspond to the chemisorbed oxygen in the metal oxides after OER [40,41]. The morphology changes of Ni-Fe-S/3NCQDs are also studied after the ORR/OER stability tests (Fig. S12a and S12b). The morphologies of Ni-Fe-S/3NCQDs basically remain the same as the original one (before the ORR/OER tests), indicating the promising mechanical stability of the porous nanocage structure. The structural stability effectively prevents the corrosion or destroying of active sites in the alkaline electrolyte to improve the long-term ORR/OER stabilities.

3.4. Zn-air battery performance for Ni-Fe-S/3NCQDs

For practical applications, Ni-Fe-S/3NCQDs electrocatalysts is employed as the air-cathode of a self-assembled rechargeable ZAB, compared with Pt/C and RuO_2 . As shown in Fig. 11a, the open-circuit voltage (OCV) of the Ni-Fe-S/3NCQDs-based ZAB is approximately 1.389 V. The maximum power densities of Ni-Fe-S/3NCQDs and Pt/C+ RuO_2 cathodes are 94 and 56 mW cm^{-2} , respectively (Fig. 11b). In Fig. S13a, the charge-discharge polarization curves show that the Ni-Fe-S/3NCQDs-based battery exhibits smaller voltage gaps between charging-discharging over the entire current density range compared with Pt/C+ RuO_2 -based ZAB, signifying a much better charge-discharge capability [77,78]. Notably, the Ni-Fe-S/3NCQDs-based battery can be efficiently charged at a higher rate because the OER overpotential usually determines the upper limit of the battery voltage during charging [79,80]. Due to the excellent OER activity of the co-existed iron and nickel hydroxides, the charging voltage of Ni-Fe-S/3NCQDs-based battery is kept at a low level. Moreover, in Fig. 11c, the specific capacities of Ni-Fe-S/3NCQDs-based ZAB at different current densities are 845.27 (at 10 mA cm^{-2}), 789.96 (at 30 mA cm^{-2}), 646.943 $\text{mAh g}^{-1}\text{Zn}$ (at 50 mA cm^{-2}).

Based on the promising charge/discharge performance of Ni-Fe-S/3NCQDs-based ZAB, its cycling stability is further investigated

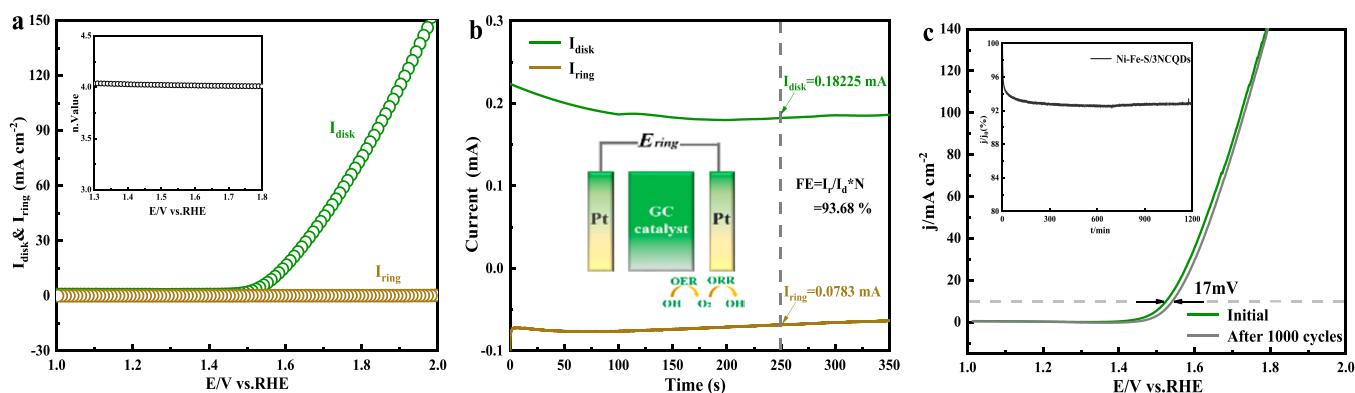


Fig. 9. Voltammogram for Ni-Fe-S/3NCQDs in 0.1 M KOH on a RRDE (1600 rpm) device and the inset shows the corresponding electron transfer number (n) as a function of applied potentials (a); Faradaic efficiency of Ni-Fe-S/3NCQDs on a RRDE (1600 rpm) device (ring potential of 0.4 V vs. RHE) (b); OER polarization curves of Ni-Fe-S/3NCQDs before and after the continuous operation in the 0.1 M KOH at 1600 rpm (inset shows the chronoamperometric (i - t) responses of Ni-Fe-S/3NCQDs in 0.1 M KOH at 1600 rpm) (c).

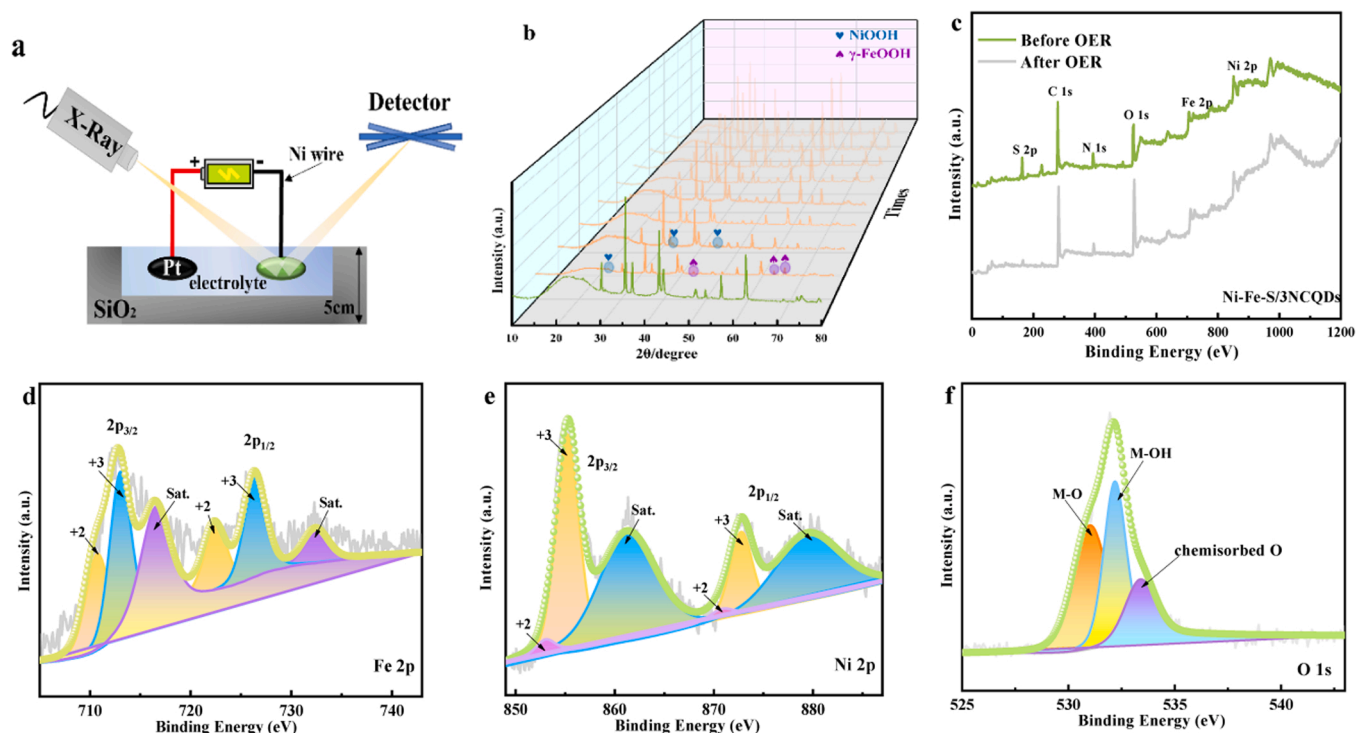


Fig. 10. Schematic diagram of the X-ray diffractometer equipped with a two-electrode electrolysis system for in situ XRD measurement (a); In situ XRD patterns of Ni-Fe-S/3NCQDs collected during OER (b); XPS survey spectra (c) and high resolution XPS spectra of Fe 2p (d), Ni 2p (e) and O 1s (f) after OER tests.

(Fig. 11d and Fig. S13b). When the cycling test is performed at 10.0 mA cm^{-2} for 1700 h (40 min per cycle), the initial discharge and charge voltages are approximately 1.19 and 2.11 V, respectively, with a voltage gap of 0.92 V and a round-trip efficiency of 56.3 %. After 360 discharge/charge cycles, the voltage gap increases slightly (only 1.27 V) and the energy efficiency decreases slightly (44.4 %). Notably, at the 82th cycle, the Pt/C+RuO₂-based ZAB shows an undesirable increase in the voltage gap (from 0.84 to 1.29 V) and a significant decrease in energy efficiency (from 56.2 % to 45.2 %). It shows that the Ni-Fe-S/3NCQDs electrocatalyst has an excellent catalytic stability in ZAB. As shown in Table S10, the cycling stability of Ni-Fe-S/3NCQDs in ZAB is higher than those of many recently-reported transition metals-based catalysts.

3.5. Origins of the superior ORR/OER catalytic activities of Ni-Fe-S/3NCQDs

Generally, the variance index $\Delta E = E_{j=10} - E_{1/2}$ is used to evaluate the bifunctional catalytic activity of the catalyst. A smaller the ΔE value means a higher electrochemical activity and a smaller energy loss. The LSV curve of Ni-Fe-S/3NCQDs exhibits a good bifunctional catalytic behavior ($\Delta E = 0.675 \text{ V}$) in the potential range of 0.3–1.7 V (Fig. 12a), which is better than most of recently-reported catalysts (Tables S11 and S12). According to the literatures, the FeS prefers a direct $4e^-$ pathway and also has the good reduction ability of H₂O₂, indicating that the ORR is more kinetically favored on the FeS [40,54,78]. Moreover, the hydrophilicity of FeS can further diminish the interface resistance for oxygen adsorption on Ni-Fe-S/xNCQDs, leading to an enhancement of the ORR activity [63]. In addition, the incorporation of NCQDs can not only enhance the effective electron transfer, but also provide additional positive active sites (N species) to optimize the adsorption capacity of O-intermediates to synergistically increase the catalytic efficiency [63, 71]. Last but not least, the interconnected porous structure of the Ni-Fe-S/xNCQDs catalyst can accelerate the effective transport of electrolyte ions and ORR-related substances, and expose more accessible active sites, thus leading to the optimal activity for ORR [33,47].

Moreover, the encapsulation of a large number of NCQDs particles in Ni-Fe-S nanocages can greatly alleviate the aggregating tendency of monodisperse NCQDs particles during continuous operation, which facilitates the durability of active sites and the prevention of methanol corrosion [28,43].

For OER, the reaction sites including the Fe sites in the FeOOH (active intermediate) and the Ni sites in NiOOH (active intermediate) are considered in the OER process. The corresponding reaction steps are shown in the Equation S2. It has been reported that due to the relatively electronegativity of transition metal, the formation of iron or nickel oxyhydroxide can enhance the charge transfer process. The strong solid-solid interfacial interactions between NiOOH and FeOOH nanoparticles in Ni-Fe-S/3NCQDs can favorably facilitate the OER procedure [71, 81–83]. As reported previously, the high-oxidative-state Fe³⁺ species in FeOOH (Fe³⁺ is most likely adsorbed at the edge or defects of Ni (II)-based catalyst) can form the oxygen bridges (such as Fe³⁺-O-Ni²⁺) under the interface interaction, which can adjust the local electronic structure of Ni²⁺ species in Ni-Fe-S/3NCQDs [33]. This interfacial interaction is found to produce a partial activation effect on charge transfer to reedit their electrochemical catalytic behaviors favorably. The synergistic interaction of Fe and Ni atoms can stabilize the OER intermediates (*OH, *O and *OOH) on the metal sites, and the OH⁻ adsorption at the Fe site is more preferable than at the Ni site [78]. However, the deprotonation of *OOH to form O₂ molecules is thermodynamically more tend to occur at the Ni site [78]. Thus, the strong electronic coupling effect between NiOOH and FeOOH facilitates the electron/charge transfer and exhibits an obvious activity improvement for OER [44,78,80]. In addition, the porous hollow nanostructure facilitates the ready penetration of electrolyte and the formation and exposure of reactive intermediates (NiOOH/FeOOH).

4. Conclusion

In summary, the porous Ni-Fe-S/xNCQDs composites with a hollow nanocage structure are elaborately fabricated by using a selective etching-sulfuration-hydrothermal strategy. The open hollow structure of

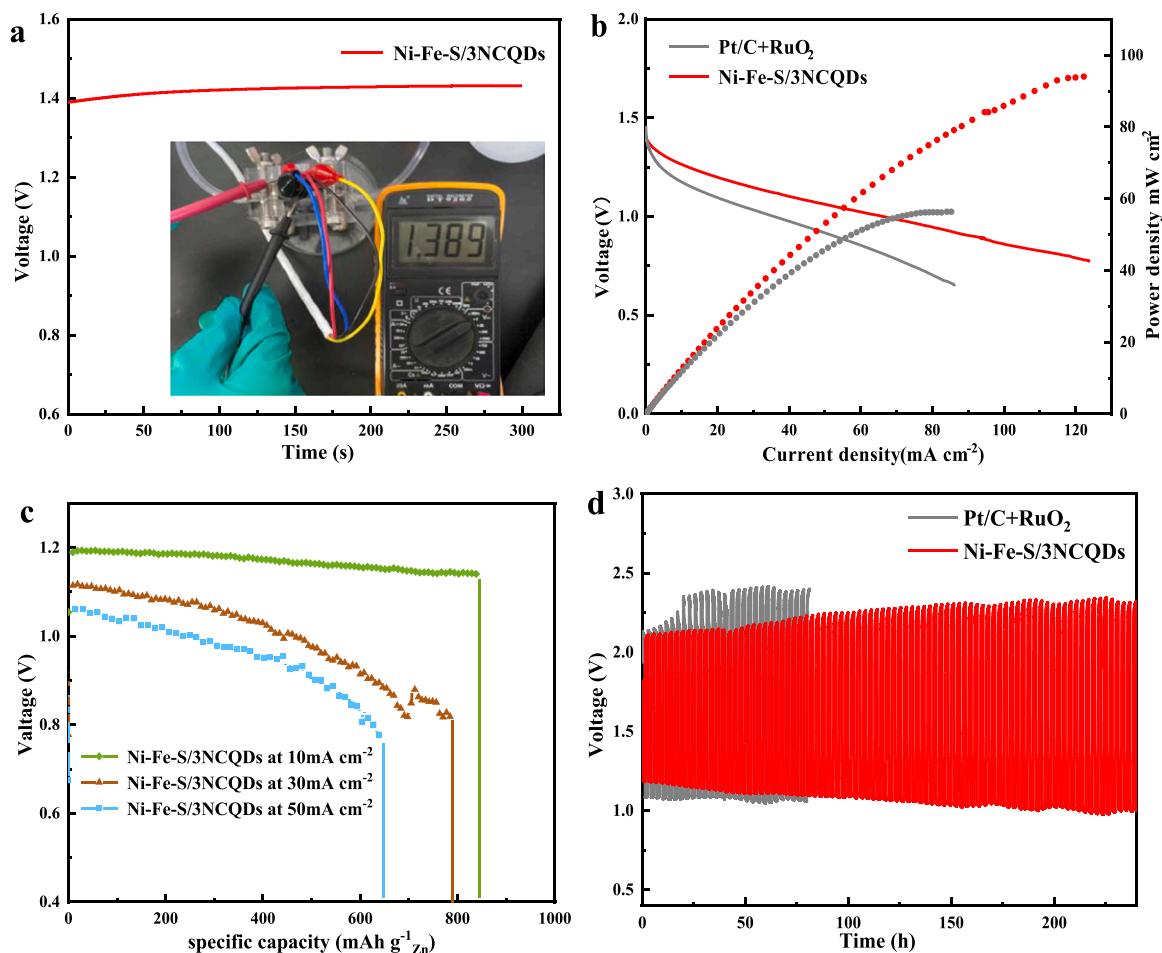


Fig. 11. Open-circuit voltage (OCV) plots (inset: photograph of Ni-Fe-S/3NCQDs-based Zn-air battery) (a); polarization and power density curves of Pt/C+RuO₂ and Ni-Fe-S/3NCQDs-based Zn-air battery (b); specific capacities at 10, 30, 50 mA cm⁻² of Ni-Fe-S/3NCQDs-based Zn-air battery (c); galvanostatic discharge-charge cycling profiles of the Pt/C+RuO₂ and Ni-Fe-S/3NCQDs-based Zn-air batteries at 10 mA cm⁻² (d).

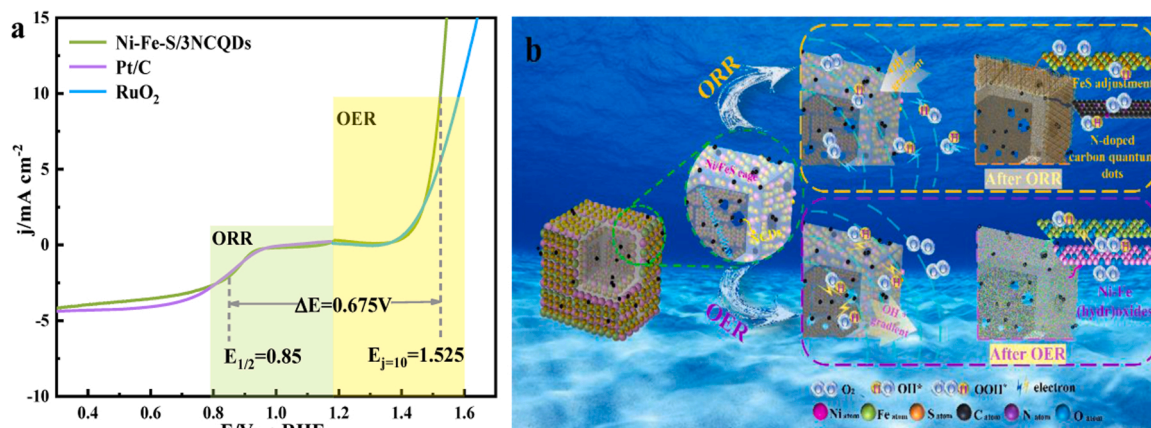


Fig. 12. Polarization curves of Ni-Fe-S/3NCQDs and Pt/C (or RuO₂) catalysts using the three-electrode system in the full OER/ORR region in O₂-saturated 0.1 M KOH solution (a); Mechanisms of oxygen reduction and oxygen evolution on Ni-Fe-S/3NCQDs (b).

cubic cage-shaped Ni-Fe-S/xNCQDs obtains a high SSA value of 478.35 m² g⁻¹. The Ni-Fe-S/3NCQDs shows a better half-wave potential (0.851 V) than commercial Pt/C (0.841 V), and a satisfactory stability ($\Delta E_{1/2} = 12.8$ mV, after 5000 cycles) for ORR in alkaline media. The promising ORR activity originates from the enhanced adsorption affinity for O₂ by the intrinsic characteristics of FeS/NiS and NCQDs, and the superior mass-transfer capability is promoted by the hollow nanocage

structure. At 10 mA cm⁻², Ni-Fe-S/3NCQDs also shows a low over-potential of 0.295 V and a Faraday efficiency of 93.68 % for OER. The synergistic effect between NiOOH and FeOOH greatly promotes the charge transfer and catalytic activity for OER. Wide reaction space and abundant mass transfer channels are conducive to the exposure of more active sites (ORR/OER) on the surface of Ni-Fe-S/3NCQDs to gain a promising bifunctional activity ($\Delta E = 0.675$ V), and the cage structure

prevents the active species from aggregation to ensure the long-term stability. Moreover, the Ni-Fe-S/3NCQDs-based rechargeable ZAB exhibits a high specific capacity of 845.27 mAh g⁻¹ Zn at 10.0 mA cm⁻², a peak power density of 94 mW cm⁻² at 93.9 mA cm⁻², and a remarkable cyclability for 360 cycles at 10.0 mA cm⁻². We believe that this study will inspire a rational design for highly active and stable bifunctional bimetal-sulfides electrocatalysts with a hollow structure.

CRedit authorship contribution statement

Rongyue Wang: Conceptualization, Methodology, Software, Investigation, Writing – original draft. **Jin Liu:** Validation, Formal analysis, Visualization. **Jiahao Xie:** Validation, Formal analysis, Visualization. **Zhuang Cai:** Resources, Writing – review & editing, Supervision, Data curation. **Yuan Yu:** Validation, Software. **Zixuan Zhang:** Validation, Software. **Xin Meng:** Validation, Formal analysis. **Cheng Wang:** Resources, Writing – review & editing, Supervision, Data curation. **Xiao-qin Xu:** Validation, Formal analysis. **Jinlong Zou:** Resources, Writing – review & editing, Supervision, Data curation.

Declaration of Competing Interest

The authors declare that they have no known competing financial interests or personal relationships that could have appeared to influence the work reported in this paper.

Data availability

Data will be made available on request.

Acknowledgements

We acknowledge the support by National Natural Science Foundation of China (52070074, 21806031 and 51578218), Outstanding Youth Fund of Heilongjiang Province (JQ2022E005), Longjiang Scholars Program (Q201912).

Appendix A. Supporting information

Supplementary data associated with this article can be found in the online version at [doi:10.1016/j.apcatb.2022.122230](https://doi.org/10.1016/j.apcatb.2022.122230).

References

- [1] B. Wei, Z.H. Fu, D. Legut, T.C. Germann, S.Y. Du, H.J. Zhang, J.S. Francisco, R. F. Zhang, Rational design of highly stable and active mxene-based bifunctional ORR/OER double-atom catalysts, *Adv. Mater.* 33 (2021) 22102595, <https://doi.org/10.1002/adma.202102595>.
- [2] M.Y. Liu, X.D. Xiao, Q. Li, L.Y. Luo, M.H. Ding, B. Zhang, Y.X. Li, J.L. Zou, B. J. Jiang, Recent progress of electrocatalysts for oxygen reduction in fuel cells, *J. Colloid Interface Sci.* 607 (2022) 791–815, <https://doi.org/10.1016/j.jcis.2021.09.008>.
- [3] S.S. Li, X.G. Hao, A. Abudula, G.Q. Guan, Nanostructured Co-based bifunctional electrocatalysts for energy conversion and storage: current status and perspectives, *J. Mater. Chem. A* 7 (2019) 18674–18707, <https://doi.org/10.1039/c9ta04949e>.
- [4] Y. Zhao, Z. Pei, X.F. Lu, D. Luan, X. Wang, X.W. Lou, Rationally designed nitrogen-doped carbon macroporous fibers with loading of single cobalt sites for efficient aqueous Zn-CO₂ batteries, *Chem. Catal.* 2 (2022) 1480, <http://doi.org.10.1016/j.checcat.2022.05.015>.
- [5] Y. Feng, K.X. Song, W. Zhang, X.Y. Zhou, S.J. Yoo, J.G. Kim, S.F. Qiao, Y.G. Qi, X. Zou, Z.J. Chen, T.T. Qin, N.L. Yue, Z.Z. Wang, D.B. Li, W.T. Zheng, Efficient ORR catalysts for zinc-air battery: Biomass-derived ultra-stable Co nanoparticles wrapped with graphitic layers via optimizing electron transfer, *J. Energy Chem.* 70 (2022) 211–218, <https://doi.org/10.1016/j.jechem.2022.01.047>.
- [6] C.X. Zhao, J.N. Liu, J. Wang, C. Wang, X. Guo, X.Y. Li, X. Chen, L. Song, B.Q. Li, Q. Zhang, A clicking confinement strategy to fabricate transition metal single-atom sites for bifunctional oxygen electrocatalysis, *Sci. Adv.* 8 (2022) eabn5091, <http://doi.org.10.1126/sciadv.abn5091>.
- [7] Y.W. Li, W.J. Zhang, J. Li, H.Y. Ma, H.M. Du, D.C. Li, S.N. Wang, J.Sh Zhao, J. M. Dou, L.Q. Xu, Fe-MOF-derived efficient ORR/OER bifunctional electrocatalyst for rechargeable zinc-air batteries, *ACS Appl. Mater. Interfaces* 12 (2020) 44710–44719, <https://doi.org/10.1021/acsami.0c11945>.
- [8] S.H. Chae, A. Muthurasu, T. Kim, J.S. Kim, M.S. Khil, M.J. Lee, H.J. Kim, Y. Lee, H. Y. Kim, Templated fabrication of perfectly aligned metal-organic framework-supported iron-doped copper-cobalt selenide nanostructure on hollow carbon nanofibers for an efficient trifunctional electrode material, *Appl. Catal. B* 293 (2021), 120209, <https://doi.org/10.1016/j.apcatb.2021.120209>.
- [9] Z.W. Chen, L.X. Chen, C.C. Yang, Q. Jiang, Atomic (single, double, and triple atoms) catalysis: frontiers, opportunities, and challenges, *J. Mater. Chem. A* 7 (2019) 3492–3515, <https://doi.org/10.1039/c8ta11416a>.
- [10] R.J. Gao, J. Wang, Z.F. Huang, R.R. Zhang, W. Wang, L. Pan, J.F. Zhang, W.K. Zhu, X.W. Zhang, C.X. Shi, J.W. Lim, J.J. Zou, Pt/Fe₂O₃ with Pt-Fe pair sites as a catalyst for oxygen reduction with ultralow Pt loading, *Nat. Energy* 6 (2021) 614–623, <http://doi.org.10.1038/s41560-021-00826-5>.
- [11] K. Song, Y. Feng, W. Zhang, W.T. Zheng, MOFs fertilized transition-metallic single-atom electrocatalysts for highly-efficient oxygen reduction: spreading the synthesis strategies and advanced identification, *J. Energy Chem.* 67 (2022) 391–422, <https://doi.org/10.1016/j.jechem.2021.10.011>.
- [12] P.S. Li, M.Y. Wang, X.X. Duan, L.R. Zheng, X.P. Cheng, Y.F. Zhang, Y. Kuang, Y. P. Li, Q. Ma, Z.X. Feng, W. Liu, X.M. Sun, Boosting oxygen evolution of single-atomic ruthenium through electronic coupling with cobalt-iron layered double hydroxides, *Nat. Commun.* 10 (2019) 1711, <https://doi.org/10.1038/s41467-019-09666-0>.
- [13] L. Du, G.X. Zhang, X.H. Liu, A. Hassanpour, M. Dubois, A.C. Tavares, S.H. Sun, Biomass-derived nonprecious metal catalysts for oxygen reduction reaction: the demand-oriented engineering of active sites and structures, *Carbon Energy* 2 (2020) 561–581, <https://doi.org/10.1002/cey2.73>.
- [14] P. Li, H.L. Wang, Recent advances in carbon-supported iron group electrocatalysts for the oxygen reduction reaction, *New Carbon Mater.* 36 (2021) 665–680, [https://doi.org/10.1016/s1872-5805\(21\)60072-0](https://doi.org/10.1016/s1872-5805(21)60072-0).
- [15] X.F. Lu, B.Y. Xia, S.Q. Zang, X.W. Lou, Metal-organic frameworks based electrocatalysts for the oxygen reduction reaction, *Angew. Chem. Int. Ed.* 59 (2020) 4634–4650, <https://doi.org/10.1002/anie.201910309>.
- [16] J.W. Woo, J.S. Lim, J.H. Kim, S.H. Joo, Heteroatom-doped carbon-based oxygen reduction electrocatalysts with tailored four-electron and two-electron selectivity, *ChemComm* 57 (2021) 7350–7361, <https://doi.org/10.1039/d1cc02667d>.
- [17] K.X. Song, Y. Feng, X.Y. Zhou, T.T. Qin, X. Zou, Y.G. Qi, Z.J. Chen, J.C. Rao, Z. Z. Wang, N.L. Yue, X. Ge, W. Zhang, W.T. Zheng, Exploiting the trade-offs of electron transfer in MOF-derived single Zn/Co atomic couples for performance-enhanced zinc-air battery, *Appl. Catal. B* 316 (2022), 121591, <https://doi.org/10.1016/j.apcatb.2022.121591>.
- [18] D.Z. Ren, J. Ying, M.L. Xiao, Y.P. Deng, J.H. Ou, J.B. Zhu, G.H. Liu, Y. Pei, S. Li, A. M. Jauhar, H.L. Jin, S. Wang, D. Su, A.P. Yu, Z.W. Chen, Hierarchically porous multimetal-based carbon nanorod hybrid as an efficient oxygen catalyst for rechargeable zinc-air batteries, *Adv. Funct. Mater.* 30 (2020) 1908167, <https://doi.org/10.1002/adfm.201908167>.
- [19] B.B. Yuan, C.Q. Li, L.H. Guan, K. Li, Y.Q. Lin, Prussian blue analog nanocubes tuning synthesis of coral-like Ni₃S₂@Ni₃(NiFeCo) core-shell nanowires array and boosting oxygen evolution reaction, *J. Power Sources* 451 (2020), 227295, <https://doi.org/10.1016/j.jpowsour.2019.227295>.
- [20] M.H. Kahnemouei, S. Shahrokhian, Mesoporous nanostructured composite derived from thermal treatment CoFe prussian blue analogue cages and electrodeposited NiCoS as an efficient electrocatalyst for an oxygen evolution reaction, *ACS Appl. Mater. Interfaces* 12 (2020) 16250–16263, <https://doi.org/10.1021/acsami.9b21663>.
- [21] J.Z. Huang, P. Xu, T.L. Gao, J.S. Huangfu, X.J. Wang, S.W. Liu, Y.M. Zhang, B. Song, Controlled synthesis of hollow bimetallic prussian blue analog for conversion into efficient oxygen evolution electrocatalyst, *ACS Sustain. Chem. Eng.* 8 (2020) 1319–1328, <https://doi.org/10.1021/acssuschemeng.9b07122>.
- [22] X. Wang, A. Dong, Z.Y. Zhu, L.L. Chai, J.Y. Ding, L. Zhong, T.T. Li, Y. Hu, J.J. Qian, S.M. Huang, Surfactant-mediated morphological evolution of MnCo prussian blue structures, *Small* 16 (2020) 2004614, <https://doi.org/10.1002/smll.202004614>.
- [23] W. Zhang, C. Wang, L.H. Guan, M.H. Peng, K. Li, Y.Q. Lin, A non-enzymatic electrochemical biosensor based on Au@PBA(Ni-Fe):MoS₂ nanocubes for stable and sensitive detection of hydrogen peroxide released from living cells, *J. Mater. Chem. B* 7 (2019) 7704–7712, <https://doi.org/10.1039/c9tb02059d>.
- [24] H.Y. Yang, J.X. Liu, Z.L. Chen, R.R. Wang, B. Fei, H.X. Liu, Y.H. Guo, R.B. Wu, Unconventional bi-vacancies activating inert Prussian blue analogues nanocubes for efficient hydrogen evolution, *Chem. Eng. J.* 420 (2021), 127671, <https://doi.org/10.1016/j.cej.2020.127671>.
- [25] M.H. Kahnemouei, S. Shahrokhian, Mesoporous nanostructured composite derived from thermal treatment CoFe prussian blue analogue cages and electrodeposited NiCoS as an efficient electrocatalyst for an oxygen evolution reaction, *ACS Appl. Mater. Interfaces* 12 (2020) 16250–16263, <https://doi.org/10.1021/acsami.9b21403>.
- [26] F. Razmjooei, K.P. Singh, D.S. Yang, W. Cui, Y.H. Jang, J.S. Yu, Fe-treated heteroatom (S/N/B/P)-doped graphene electrocatalysts for water oxidation, *ACS, Catalysis* 7 (2017) 2381–2391, <http://doi.org.10.1021/acscatal.6b03291>.
- [27] S. Jin, Are metal chalcogenides, nitrides, and phosphides oxygen evolution catalysts or bifunctional catalysts? *ACS Energy Lett.* 2 (2017) 1937–1938, <http://doi.org.10.1021/acsenenergylett.7b00679>.
- [28] Y.T. Huang, W.G. Liao, Hierarchical carbon material of N-doped carbon quantum dots in-situ formed on N-doped carbon nanotube for efficient oxygen reduction, *Appl. Surf. Sci.* 495 (2019), 143597, <https://doi.org/10.1016/j.apsusc.2019.143597>.
- [29] X.F. Lu, Y. Chen, S. Wang, S. Gao, X.W.D. Lou, Interfacing manganese oxide and cobalt in porous graphitic carbon polyhedrons boosts oxygen electrocatalysis for

- Zn-air batteries, *Adv. Mater.* 31 (2019), 1902339 <http://doi.org/10.1002/adma.201902339>.
- [30] K.K. Huang, Y. Sun, Y. Zhang, X.Y. Wang, W. Zhang, S.H. Feng, Hollow-structured metal oxides as oxygen-related catalysts, *Adv. Mater.* 31 (2019), 1801430, <https://doi.org/10.1002/adma.201801430>.
- [31] D.Z. Ren, J. Ying, M.L. Xiao, Y.P. Deng, J.H. Ou, J.B. Zhu, G.H. Liu, Y. Pei, S. Li, A. M. Jauhar, H.L. Jin, S. Wang, D. Su, A.P. Yu, Z.W. Chen, Hierarchically porous multimetal-based carbon nanorod hybrid as an efficient oxygen catalyst for rechargeable zinc-air batteries, *Adv. Funct. Mater.* 30 (2020), 1908167, <https://doi.org/10.1002/adfm.201908167>.
- [32] Z.B. Liang, W.Y. Zhou, S. Gao, R. Zhao, H. Zhang, Y.Q. Tang, J.Q. Cheng, T.J. Qiu, B.J. Zhu, C. Qu, W.H. Guo, Q. Wang, R.Q. Zou, Fabrication of hollow CoP/TiO_x heterostructures for enhanced oxygen evolution reaction, *Small* 16 (2020), 1905075, <https://doi.org/10.1002/smll.201905075>.
- [33] J.W. Nai, Y. Lu, L. Yu, X. Wang, X.W. Lou, Formation of Ni-Fe mixed diselenide nanocages as a superior oxygen evolution electrocatalyst, *Adv. Mater.* 29 (2017), 1703874, <https://doi.org/10.1002/adma.201703870>.
- [34] D.L. Chen, Z.M. Xu, W. Chen, G.L. Chen, J. Huang, C.S. Song, C.R. Li, K. Ostrikov, Just add water to split water: ultrahigh-performance bifunctional electrocatalysts fabricated using eco-friendly heterointerfacing of NiCo diselenides, *J. Mater. Chem. A* 8 (2020) 12035–12044, <https://doi.org/10.1039/d0ta02121k>.
- [35] T.Z. Jiang, P. Dai, W. Zhang, M.Z. Wu, Fish bone-derived N, S co-doped interconnected carbon nanofibers network coupled with (Fe, Co, Ni)₉S₈ nanoparticles as efficient bifunctional electrocatalysts for rechargeable and flexible all-solid-state Zn-air battery, *Electrochim. Acta* 373 (2021), 137903, <https://doi.org/10.1016/j.electacta.2021.137903>.
- [36] K. Liu, Z.Y. Zhu, M.Q. Jiang, L.C. Li, L.F. Ding, M. Li, D.M. Sun, G.X. Yang, G.T. Fu, Y.W. Zhang, Boosting electrocatalytic oxygen evolution over Ce–Co₂S₈ core-shell nanoneedle arrays by electronic and architectural dual engineering, *Chem. Eur. J.* 28 (2022), e202200664 <http://doi.org/10.1002/chem.202200664>.
- [37] K. Wan, J.S. Luo, X. Zhang, C. Zhou, J.W. Seo, P. Subramanian, J.W. Yan, J. Fransaer, P. Subramanian, J.W. Yan, J. Fransaer, A template-directed bifunctional NiS_x/nitrogen-doped mesoporous carbon electrocatalyst for rechargeable Zn-air, *Batter., J. Mater. Chem. A* 7 (2019) 19889–19897, <https://doi.org/10.1039/c9ta06446j>.
- [38] B. Fei, Z.L. Chen, J.X. Liu, H.B. Xu, X.X. Yan, H.L. Qing, M. Chen, R.B. Wu, Ultrathinning nickel sulfide with modulated electron density for efficient water splitting, *Adv. Energy Mater.* 10 (2020) 2001963, <https://doi.org/10.1002/aenm.202001963>.
- [39] T.W. Wu, Y.R. Wang, H.B. Zhao, J.P. Dong, J.Q. Xu, J. Si doped Fe-N/C catalyst for oxygen reduction reaction directed by ordered mesoporous silica nanospheres template strategy, *Colloid Interface Sci.* 603 (2021) 706–715, <https://doi.org/10.1016/j.jcis.2021.06.116>.
- [40] Y.B. Sun, Y. Li, S.J. You, X.R. Li, Y. Zhang, Z. Cai, M.Y. Liu, N.Q. Ren, J.L. Zou, Fe₃C/CoFe₂O₄ nanoparticles wrapped in one-dimensional MIL-53 (Fe)-derived carbon nanofibers as efficient dual-function oxygen catalysts, *Chem. Eng. J.* 424 (2021), 130460, <https://doi.org/10.1016/j.cej.2021.130460>.
- [41] Y. Zhang, Y.B. Sun, Z. Cai, S.J. You, X.R. Li, Y.H. Zhang, Y. Yu, N.Q. Ren, J.L. Zou, Stable CuO with variable valence states cooperated with active Co²⁺ as catalyst/co-catalyst for oxygen reduction/methanol oxidation reactions, *J. Colloid Interface Sci.* 593 (2021) 345–358, <https://doi.org/10.1016/j.jcis.2021.02.125>.
- [42] J.H. Li, S.J. You, M.Y. Liu, P. Zhang, Y. Dai, Y. Yu, N.Q. Ren, J.L. Zou, ZIF-8-derived carbon-thin-layer protected WC/W₂O₆ micro-sized rods with enriched oxygen vacancies as efficient Pt co-catalysts for methanol oxidation and oxygen reduction, *Appl. Catal. B* 265 (2020), 118574, <https://doi.org/10.1016/j.apcatb.2019.118574>.
- [43] R.Y. Wang, B. Liu, S.J. You, Y. Li, Y. Zhang, D. Wang, B. Tang, Y.B. Sun, J.L. Zou, Three-dimensional Ni₃Se₄ flowers integrated with ultrathin carbon layer with strong electronic interactions for boosting oxygen reduction/evolution reactions, *Chem. Eng. J.* 430 (2022), 132720, <https://doi.org/10.1016/j.cej.2021.132720>.
- [44] A. McKee, A. Samanta, A. Rassoolkhani, J. Koonce, W.J. Huang, J. Fields, S. K. Shaw, J. Gomes, H.T. Ding, S. Mubeen, Effect of silver electrode wetting state on oxygen reduction electrochemistry, *ChemComm* 57 (2021) 8003–8006, <https://doi.org/10.1039/d1cc01438b>.
- [45] L.L. Chen, X.L. Xu, W.X. Yang, J.B. Jia, Recent advances in carbon-based electrocatalysts for oxygen reduction reaction, *Chin. Chem. Lett.* 31 (2020) 626–634, <https://doi.org/10.1016/j.ccl.2019.08.008>.
- [46] B. Liu, R.Y. Wang, Y. Yao, J. Ma, Y.B. Sun, J.F. Wan, Y. Zhang, S.Q. Wang, J.L. Zou, Hollow-structured CoP nanotubes wrapped by N-doped carbon layer with interfacial charges polarization for efficiently boosting oxygen reduction/evolution reactions, *Chem. Eng. J.* 431 (2022), 133238, <https://doi.org/10.1016/j.cej.2021.133238>.
- [47] X.F. Lu, S.L. Zhang, E. Shangguan, P. Zhang, S.Y. Gao, X.W. Lou, Nitrogen-doped cobalt pyrite yolk-shell hollow spheres for long-life rechargeable Zn-air batteries, *Adv. Sci.* 7 (2020) 2001178, <https://doi.org/10.1002/advs.202001178>.
- [48] X. Liu, Y.Q. Li, Z.Y. Cao, Z.H. Yin, T.L. Ma, S.R. Chen, Current progress of metal sulfides derived from metal-organic frameworks for advanced electrocatalysis: potential electrocatalysts with diverse applications, *J. Mater. Chem. A* 10 (2022) 1617–1641, <https://doi.org/10.1039/d1ta09925f>.
- [49] D.M. Morales, M.A. Kazakova, S. Dieckhoefer, A.G. Selyutin, G.V. Golubtsov, V. Schuhmann, J. Masa, Trimetallic Mn-Fe-Ni oxide nanoparticles supported on multi-walled carbon nanotubes as high-performance bifunctional ORR/OER electrocatalyst in alkaline media, *Adv. Funct. Mater.* 30 (2020) 1905992, <https://doi.org/10.1002/adfm.201905992>.
- [50] Y. Huang, S.L. Zhang, X.F. Lu, Z.P. Wu, D.Y. Luan, X.W. Lou, Trimetallic spinel NiCo₂-xFe_xO₄ nanoboxes for highly efficient electrocatalytic oxygen evolution, *Angew. Chem. Int. Ed.* 60 (2021) 11841–11846, <https://doi.org/10.1002/anie.202103058>.
- [51] Y.J. Fang, D.Y. Luan, S.Y. Gao, X.W. Lou, Rational design and engineering of one-dimensional hollow nanostructures for efficient electrochemical energy storage, *Angew. Chem. Int. Ed.* 60 (2021) 20102–20118, <https://doi.org/10.1002/anie.202104401>.
- [52] J.Y. Feng, R.S. Cai, E. Magliocca, H. Luo, L.K. Higgins, G.L.F. Romario, X.Q. Liang, A. Pedersen, Z. Xu, Z.Y. Guo, A. Periasamy, D. Brett, T.S. Miller, S.J. Haigh, B. Mishra, M. Titirici, M. Iron, Nitrogen Co-doped carbon spheres as low cost, scalable electrocatalysts for the oxygen reduction reaction, *Adv. Funct. Mater.* 31 (2021) 2102974, <https://doi.org/10.1002/adfm.202102974>.
- [53] H.G. Jo, K.H. Kim, H.J. Ahn, Nitrogen-doped carbon quantum dots decorated on platinum catalysts for improved oxygen reduction reaction, *Appl. Surf. Sci.* 554 (2021), 149594, <https://doi.org/10.1016/j.apsusc.2021.149594>.
- [54] X. Zhu, D. Zhang, C.J. Chen, Q. Zhang, R.S. Liu, Z. Xia, L. Dai, R. Amal, X. Lu, Harnessing the interplay of Fe-Ni atom pairs embedded in nitrogen-doped carbon for bifunctional oxygen electrocatalysis, *Nano Energy* 71 (2020), 104597, <https://doi.org/10.1016/j.nanoen.2020.104597>.
- [55] F.H.K. Pan, T. Jin, W.W. Yang, H. L. Y. Q. Cao, J. Hu, X.G. Zhou, H.L. Liu, X. Z. Duan, Theory-guided design of atomic Fe–Ni dual sites in N,P-co-doped C for boosting oxygen evolution reaction, *Chem. Catal.* 19 (2021) 734–745, <http://doi.org/10.1016/j.checat.2021.06.017>.
- [56] Y.D. Xu, Y.J. Yan, M.Y. Pang, L.W. Wang, Y.X. Zhao, C.S. Deng, Y. Cui, X.K. Guo, P. Wang, W.P. Ding, A surface regulation strategy to fabricate Cu-Nx sites of high homogeneity with countable activity towards oxygen reduction, *Appl. Surf. Sci.* 560 (2021), 150054, <https://doi.org/10.1016/j.apsusc.2021.150054>.
- [57] Y. Qin, W. Zhang, K. Guo, X. Liu, J. Liu, X. Liang, X. Wang, D. Gao, L. Gan, Y. Zhu, Z. Zhang, W. Hu, Fine-tuning intrinsic strain in penta-twinned Pt–Cu–Mn nanoframes boosts oxygen reduction catalysis, *Adv. Funct. Mater.* 30 (2020) 1910107, <http://doi.org/10.1002/adfm.201910107>.
- [58] G.W. Sievers, A.W. Jensen, J. Quinson, A. Zana, F. Bizzotto, M. Oezaslan, A. Dworak, J.J.K. Kirkensgaard, T.E.L. Smithuysen, S. Kadkhodazadeh, M. Juelsholt, K.M.Ø. Jensen, K. Anklam, H. Wan, J. Schäfer, K. C  pe, M. Escudero-Escribano, J. Rossmeisl, A. Quade, V. Br  ser, M. Arenz, Self-supported Pt–CoO networks combining high specific activity with high surface area for oxygen reduction, *Nat. Mater.* 20 (2020) 208–213, <http://doi.org/10.1038/s41563-020-0775-8>.
- [59] X.R. Wang, J.Y. Liu, Z.W. Liu, W.C. Wang, J. Luo, X.P. Han, X.W. Du, S.Z. Qiao, J. Yang, Identifying the key role of pyridinic–N–Co bonding in synergistic electrocatalysis for reversible ORR/OER, *Adv. Mater.* 30 (2018), 1800005 <http://doi.org/10.1002/adma.201800005>.
- [60] K. Amini, J. Gostick, M.D. Pritzker, Metal and metal oxide electrocatalysts for redox flow batteries, *Adv. Funct. Mater.* 30 (2020), 1910564 <http://doi.org/10.1002/adfm.201910564>.
- [61] W.C. Wan, C.A. Triana, J.G. Lan, J.G. Li, C.S. Allen, Y.G. Zhao, M. Iannuzzi, G. R. Patzke, Bifunctional single atom electrocatalysts: coordination-performance correlations and reaction pathways, *ACS Nano* 14 (2020) 13279–13293, <https://doi.org/10.1021/acsnano.0c05088>.
- [62] V. Imandi, A. Chatterjee, Effect of surface Ni on oxygen reduction reaction in dealloyed nanoporous Pt–Ni, *Ind. Eng. Chem. Res.* 58 (2019) 7438–7447, <https://doi.org/10.1021/acs.iecr.8b05204>.
- [63] A. Tyagi, K.K. Kar, H. Yokoi, Atomically dispersed Ni/Ni_xS_y anchored on doped mesoporous networked carbon framework: boosting the ORR performance in alkaline and acidic media, *J. Colloid Interface Sci.* 571 (2020) 285–296, <https://doi.org/10.1016/j.jcis.2020.03.043>.
- [64] Z.R. Chen, R.L. Liu, S.H. Liu, J.L. Huang, L.Y. Chen, R. Nadimicherla, D.C. Wu, R. Wu, FeS/FeNC decorated N,S-co-doped porous carbon for enhanced ORR activity in alkaline media, *ChemComm* 56 (2020) 12921–12924, <https://doi.org/10.1039/d0cc04749j>.
- [65] C.G. Kuai, Y. Zhang, L.L. Han, H.L.L. Xin, C.J. Sun, D. Nordlund, S.Z. Qia, X.W. Du, F. Lin, Creating compressive stress at the NiOOH/NiO interface for water oxidation, *J. Mater. Chem. A* 8 (2020) 10747–10754, <https://doi.org/10.1039/d0ta04244g>.
- [66] P. Yan, Q. Liu, H. Zhang, L.C. Qiu, H.B. Wu, X.Y. Yu, Deeply reconstructed hierarchical and defective NiOOH/FeOOH nanoboxes with accelerated kinetics for the oxygen evolution reaction, *J. Mater. Chem. A* 9 (2021) 15586–15594, <https://doi.org/10.1039/d1ta03362j>.
- [67] P.L. Zheng, Y. Zhang, Z.F. Dai, Y. Zheng, K.N. Dinh, J. Yang, R. Dangol, X.B. Liu, Q. Y. Yan, Constructing multifunctional heterostructure of Fe₂O₃@Ni₃Se₄ nanotubes, *Small* 14 (2018), 1704065, <https://doi.org/10.1002/smll.201704065>.
- [68] J.M.P. Mart  rez, E.A. Carter, Noninnocent influence of host beta-NiOOH redox activity on transition-metal dopants' efficacy as active sites in electrocatalytic water oxidation, *ACS Catal.* 10 (2020) 2720–2734, <https://doi.org/10.1021/acscatal.9b05092>.
- [69] K. Wang, W. Wu, Z.H. Tan, L.G. Li, S.W. Chen, N.M. Bedford, Hierarchically structured Co(OH)₂/CoPt/N-CN air cathodes for rechargeable zinc-air batteries, *ACS Appl. Mater. Interfaces* 11 (2019) 4983–4994, <https://doi.org/10.1021/acsaami.8b18424>.
- [70] Z.X. Yin, S. Zhang, J.L. Li, S.K. Ma, W. Chen, X.Z. Ma, Y. Zhou, Z.F. Zhang, X. Wang, In situ fabrication of a Ni-Fe-S hollow hierarchical sphere: an efficient (pre)catalyst for OER and HER, *New. J. Chem.* 45 (2021) 12996–13003, <https://doi.org/10.1039/d1nj02382a>.
- [71] F. Dionigi, P. Strasser, NiFe-based (oxy)hydroxide catalysts for oxygen evolution reaction in non-acidic electrolytes, *Adv. Energy Mater.* 6 (2016), 1600621, <https://doi.org/10.1002/aenm.201600621>.

- [72] K.X. Zhang, Y.L. Zhang, Q.H. Zhang, Z.B. Liang, L. Gu, W.H. Guo, B.J. Zhu, S. J. Guo, R.Q. Zou, Metal-organic framework-derived Fe/Cu-substituted Co nanoparticles embedded in CNTs-grafted carbon polyhedron for Zn-air batteries, *Carbon Energy* 2 (2020) 283–293, <http://doi.org/10.1002/cey2.35>.
- [73] Z.J. Li, X.D. Wu, X. Jiang, B.B. Shen, Z.S. Tian, D.M. Shen, G.T. Fu, Y.W. Tang, Surface carbon layer controllable Ni₃Fe particles confined in hierarchical N-doped carbon framework boosting oxygen evolution reaction, *Adv. Powder Mater.* 1 (2021), 10020 <http://doi.org/10.1016/j.apmate.2021.11.007>.
- [74] H. Li, X.X. Shu, P. Tong, J.H. Zhang, P.F. An, Z.X. Lv, H. Tian, J.T. Zhang, H.B. Xia, Fe-Ni alloy nanoclusters anchored on carbon aerogels as high-efficiency oxygen electrocatalysts in rechargeable Zn-air batteries, *Small* 17 (2021), 2102002, <https://doi.org/10.1002/smll.202102002>.
- [75] S.L. Zhang, B.Y. Guan, X.F. Lu, S.B. Xi, Y.H. Du, X.W. Lou, Metal atom-doped Co₃O₄ hierarchical nanoplates for electrocatalytic oxygen evolution, *Adv. Mater.* 32 (2020), 2002235, <https://doi.org/10.1002/adma.202002235>.
- [76] W.G. Fang, Z.M. Bai, X.X. Yu, W. Zhang, M.Z. Wu, Pollen-derived porous carbon decorated with cobalt/iron sulfide hybrids as cathode catalysts for flexible all-solid-state rechargeable Zn-air batteries, *Nanoscale* 12 (2020) 11746–11758, <https://doi.org/10.1039/d0nr02376k>.
- [77] Y.Y. Chen, Y. Xu, S. Niu, J. Yan, Y.Y. Wu, F.K. Du, Y.Z. Zhao, Z.R. Zhu, Z.J. Jiang, X. C. Tan, A highly efficient Fe-Ni-S/NF hybrid electrode for promoting oxygen evolution performance, *ChemComm* 57 (2021) 4572–4575, <https://doi.org/10.1039/d1cc00569c>.
- [78] X.F. Li, Y.J. Liu, H.B. Chen, M. Yang, D.G. Yang, H.M. Li, Z.Q. Lin, Rechargeable Zn-air batteries with outstanding cycling stability enabled by ultrafine FeNi nanoparticles-encapsulated N-doped carbon nanosheets as a bifunctional electrocatalyst, *Nano Lett.* 21 (2021) 3098–3105, <https://doi.org/10.1021/acs.nanolett.1c00279>.
- [79] J. Wang, J.X. Xu, X.Y. Guo, T. Shen, C.J. Xuan, B.L. Tian, Z.R. Wen, Y. Zhu, D. L. Wang, Synergistic regulation of nickel doping/hierarchical structure in cobalt sulfide for high performance zinc-air battery, *Appl. Catal. B* 298 (2021), 120539 <http://doi.org/10.1016/j.apcatb.2021.120539>.
- [80] X.F. Lu, Y.J. Fang, D.Y. Luan, X.W.D. Lou, Metal-organic frameworks derived functional materials for electrochemical energy storage and conversion: a mini review, *Nano Lett.* 21 (2021) 1555–1565, <https://doi.org/10.1021/acs.nanolett.0c04898>.
- [81] F.T. Kong, X.H. Fan, A.G. Kong, Z.Q. Zhou, X.Y. Zhang, Y.K. Shan, Covalent phenanthroline framework derived FeS@Fe₃C composite nanoparticles embedding in N-S-codoped carbons as highly efficient trifunctional electrocatalysts, *Adv. Func. Mater.* 28 (2018) 1803973, <https://doi.org/10.1002/adfm.201803973>.
- [82] W.J. Li, S. Xue, S. Watzele, S.J. Hou, J. Fichtner, A.L. Semrau, L.J. Zhou, A. Welle, A.S. Bandarenka, R.A. Fischer, Advanced bifunctional oxygen reduction and evolution electrocatalyst derived from surface-mounted metal-organic frameworks, *Angew. Chem. Int. Ed.* 59 (2020) 5837–5843, <https://doi.org/10.1002/anie.201916507>.
- [83] Q. Sun, K.X. Yao, Y.X. Zhang, MnO₂-directed synthesis of NiFe-LDH@FeOOH nanosheet arrays for supercapacitor negative electrode, *Chin. Chem. Lett.* 31 (2020) 2343–2346, <https://doi.org/10.1016/j.ccllet.2020.03.069>.